

Vortex dynamics and fractal structures in reactive and nonreactive Richtmyer–Meshkov instability

Cite as: Phys. Fluids **33**, 044114 (2021); <https://doi.org/10.1063/5.0047379>

Submitted: 12 February 2021 • Accepted: 03 April 2021 • Published Online: 27 April 2021

 M. Bambauer,  N. Chakraborty,  M. Klein, et al.

COLLECTIONS

Paper published as part of the special topic on [In Memory of Edward E. \(Ted\) O'Brien](#)



ARTICLES YOU MAY BE INTERESTED IN

Modeling the amplitude growth of Richtmyer–Meshkov instability in shock–flame interactions
Physics of Fluids **32**, 104103 (2020); <https://doi.org/10.1063/5.0021989>

Turbulent mixing and transition criteria of flows induced by hydrodynamic instabilities
Physics of Plasmas **26**, 080901 (2019); <https://doi.org/10.1063/1.5088745>

Single- and dual-mode Rayleigh–Taylor instability at microscopic scale
Physics of Fluids **33**, 042102 (2021); <https://doi.org/10.1063/5.0042505>

[LEARN MORE](#)

APL Machine Learning

Open, quality research for the networking communities

COMING SOON



Vortex dynamics and fractal structures in reactive and nonreactive Richtmyer–Meshkov instability

Cite as: Phys. Fluids 33, 044114 (2021); doi: 10.1063/5.0047379

Submitted: 12 February 2021 · Accepted: 3 April 2021 ·

Published Online: 27 April 2021



View Online



Export Citation



CrossMark

M. Bambauer,^{1,a)} N. Chakraborty,² M. Klein,¹ and J. Hasslberger¹

AFFILIATIONS

¹Bundeswehr University Munich, Department of Aerospace Engineering, 85577 Neubiberg, Germany

²Newcastle University, School of Engineering, Newcastle upon Tyne NE1 7RU, United Kingdom

Note: This paper is part of the special topic, In Memory of Edward E. (Ted) O'Brien.

^{a)}Author to whom correspondence should be addressed: maximilian.bambauer@unibw.de

ABSTRACT

Hydrodynamic instabilities caused by shock-flame interactions are a fundamental challenge in the accurate prediction of explosion loads in the context of nuclear and process plant safety. To investigate the Richtmyer–Meshkov instability, a series of three-dimensional numerical simulations of shock-flame interactions are performed, including lean, stoichiometric, and nonreactive homogeneous H₂/Air mixtures. The equivalence ratio has a strong influence on the achievable flame wrinkling and mixing, by impacting key physical parameters such as the heat release parameter, flame thickness, and reactivity. The reactivity is found to be a decisive factor in the evolution of the wrinkled flame brush, as it can cause burnout of the developing fresh gas cusps and wrinkled structures. The importance of reactivity is further emphasized by comparisons to a nonreactive case. Analysis of the enstrophy (energy equivalent of vorticity) transport terms shows that baroclinic torque is dominant during shock-flame interactions. After the shock interaction, the vortex stretching, dissipation, and dilatation terms gain in importance significantly. A power-law based modeling approach of the flame wrinkling is investigated by explicitly filtering the present simulation data. The values determined for the fractal dimension show a nonlinear dependency on the chosen equivalence ratio, whereas the inner cutoff scale is found to be approximately independent of the equivalence ratio for the investigated cases.

© 2021 Author(s). All article content, except where otherwise noted, is licensed under a Creative Commons Attribution (CC BY) license (<http://creativecommons.org/licenses/by/4.0/>). <https://doi.org/10.1063/5.0047379>

I. INTRODUCTION

The interaction of a density gradient $\nabla\rho$ as present at the interface between light and heavy fluids and a pressure gradient ∇p can lead to hydrodynamic instability, commonly referred to as the Richtmyer–Meshkov instability (RMI)^{1,2} or the Rayleigh–Taylor instability (RTI).^{3,4} In the case of RTI the pressure gradient is caused by constant (e.g. gravity) or time-varying acceleration,⁵ while the RMI is caused by the pressure gradient across a shock wave (impulsive acceleration). The misalignment of ∇p and $\nabla\rho$ leads to the production of vorticity, amplifying small disturbances across the interface and subsequently causing wrinkling and increased mixing of heavy and light fluids. An extensive review of occurrences for RMI and RTI in nature and technology, alongside common modeling approaches, has been compiled by Zhou^{6,7} and Zhou *et al.*⁸ Notable use-cases include inertial confinement fusion⁹ and the modeling of supernovae explosions.¹⁰ This work focuses on the RMI in the context of combustion, where it plays an important role as a mechanism for flame acceleration (FA) and deflagration-to-detonation transition (DDT) in geometrically

confined explosions.^{11,12} In this setting, the RMI is caused by a shock wave (∇p) interacting with a flame ($\nabla\rho$), after being reflected from an obstacle or wall.^{13,14} Figure 1 shows the mechanism, responsible for the amplification of disturbances on the flame surface after interacting with the shock wave. Notable is also the phase-reversal effect in Fig. 1 (left), which occurs when the shock wave travels from high to low density. The influence of the RMI can be a decisive factor for DDT, as it causes heavy wrinkling of the flame brush region and subsequently a strong increase in the integral reaction rate.¹⁵ In nuclear and process plant safety research, the accurate prediction of DDT and explosion loads pose a major challenge.¹⁶ The heavy computational demands caused by the wide time- and length-scale spectra, associated with the simulation of the chemistry and turbulent flow in these cases¹⁷ only allow for the qualitative prediction of explosion loads in current commercial applications. By including small-scale RMI effects via a subgrid model, the accuracy of large eddy simulations (LES) or unsteady Reynolds-averaged Navier–Stokes simulations (URANS) could be improved.¹⁸ This work focuses on the influence of the equivalence

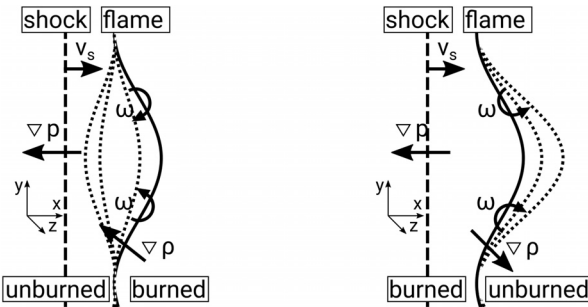


FIG. 1. Amplification of flame surface disturbance (—) and its temporal evolution (.....) due to baroclinic torque (ω) caused by the misalignment of ∇p and $\nabla \rho$. Left: shock wave (---) travels with velocity V_s from the unburned to the burned side, including phase reversal effect. Right: shock wave travels from the burned to the unburned side.

ratio on the development of the RMI by comparing shock-flame interactions of a lean and stoichiometric H₂/air-gas mixture. The equivalence ratio influences many important flame characteristics, such as flame speed, adiabatic flame temperature and flame thickness. In many reactor safety scenarios, the gas mixture is typically assumed to be lean,¹⁹ therefore analyzing and understanding the influence of these flame characteristics is important for creating a subgrid model for this use-case. An overview of the numerical methods used in the simulation is given in Sec. II, followed by an explanation of the case setup in Sec. III. The simulation results are presented in Sec. IV, which includes a discussion on the temporal development of the flame surface area A_f and mixing width δ_w (Sec. IV A) and a detailed analysis of individual terms in the enstrophy (energy-equivalent of the vorticity) transport equation in Sec. IV B. The discussion of the results is completed with Sec. IV C, investigating the fractal behavior of the wrinkled flame brush.

II. NUMERICAL METHODS

The high-fidelity 3D combustion simulation of the shock-flame interactions is carried out using the SENG_A solver.²⁰ It solves for the compressible Navier-Stokes equations, including the total energy e_t and reaction progress variable c , given by Eqs. (1a)–(1d),

$$\frac{\partial \rho}{\partial t} + \frac{\partial(\rho u_k)}{\partial x_k} = 0, \quad (1a)$$

$$\frac{\partial(\rho u_i)}{\partial t} + \frac{\partial(\rho u_k u_i)}{\partial x_k} = -\frac{\partial p}{\partial x_i} + \frac{\partial \tau_{ki}}{\partial x_k}, \quad (1b)$$

$$\begin{aligned} \frac{\partial(\rho e_t)}{\partial t} + \frac{\partial(\rho u_k e_t)}{\partial x_k} &= -\frac{\partial(p u_k)}{\partial x_k} + \frac{\partial(\tau_{ki} u_i)}{\partial x_k} + \frac{\partial}{\partial x_k} \left[\lambda \frac{\partial T}{\partial x_k} \right] \\ &\quad - \frac{\partial}{\partial x_k} \left[h \rho D \frac{\partial c}{\partial x_k} \right], \end{aligned} \quad (1c)$$

$$\frac{\partial(\rho c)}{\partial t} + \frac{\partial(\rho u_k c)}{\partial x_k} = \dot{\omega} + \frac{\partial}{\partial x_k} \left[\rho D \frac{\partial c}{\partial x_k} \right]. \quad (1d)$$

The reaction progress variable c can be defined with the fuel mass fraction Y_F ,

$$c = \frac{Y_F - Y_F^u}{Y_F^b - Y_F^u}, \quad (2)$$

where superscripts u and b denote unburnt and burnt gas quantities respectively. In fresh gases $c=0$ and in burnt gases $c=1$. Using the

specific gas constant R_s , the specific isochoric heat capacity c_v , and the specific heat of reaction H , the equations of state are

$$p = \rho R_s T, \quad (3a)$$

$$e_t = c_v(T - T_{ref}) + 0.5 u_k u_k + H(1 - c). \quad (3b)$$

The thermodynamic properties (λ , c_p , c_v , ρD) are approximated as constant (temperature independent). Usage of a detailed chemistry model would lead to large computational costs^{21,22} and is not justified for the study conducted here, since the RMI observed in this use-case is mainly dominated by the fluid dynamics of the shock-flame interaction. In the context of turbulent reactive flows, Arrhenius-type approaches are commonly found in the literature.²³ The chemical source term [$\dot{\omega}$ in Eq. (1d)] is expressed using an irreversible Arrhenius expression,

$$\dot{\omega} = \rho B(1 - c) \exp \left[\frac{-E_{ac}}{RT} \right], \quad (4)$$

where B , E_{ac} and R denote the pre-exponential factor, the activation energy and the molar gas constant. The dimensionless temperature T^* is defined as $T^* = (T - T_0)/(T_{ad} - T_0)$, where T_{ad} is the adiabatic flame temperature and T_0 is the reference temperature corresponding to the initial state of the unburned H₂/air-gas mixture. By defining the Zeldovich number as $\beta_z = E_{ac}(T_{ad} - T_0)/(RT_{ad}^2)$ and the heat release parameters $\tau_h = (T_{ad} - T_0)/T_0$ and $\alpha_h = \tau_h/(1 + \tau_h)$, Eq. (4) can be written as

$$\dot{\omega} = \rho B \exp \left[-\frac{\beta_z}{\alpha_h} \right] (1 - c) \exp \left[-\frac{\beta_z(1 - T^*)}{1 - \alpha_h(1 - T^*)} \right]. \quad (5)$$

For the cases presented in this work a constant Zeldovich number of $\beta_z = 5.0$ is assumed²⁴ and the values chosen for τ_h are listed in Table I.

The viscous stress tensor τ_{ij} is defined as

$$\tau_{ij} = \mu \left[\frac{\partial u_i}{\partial x_j} + \frac{\partial u_j}{\partial x_i} \right] - \frac{2}{3} \mu \delta_{ij} \left[\frac{\partial u_k}{\partial x_k} \right]. \quad (6)$$

Using reference values for density ρ_0 , thermal conductivity λ_0 , mass diffusivity D_0 , specific heat capacity $c_{p,0}$ respective $c_{v,0}$, and dynamic viscosity μ_0 , additional dimensionless quantities such as the

TABLE I. Input parameters for the simulation cases. The bold numbers indicate the successive changes from $\phi = 0.5$ to the parameters corresponding to $\phi = 1.0$.

Case	Le	Re ₀	τ_h	Ma ₀	A _{atw}	Ma _s	Pr	$\dot{\omega}$
$\phi = 1.0$	1.1	1093	7.1	0.005 609	0.780	1.5	0.47	Eq. (5)
$\phi = 0.875$	0.9	933	6.7	0.004 721	0.766	1.5	0.475	Eq. (5)
$\phi = 0.75$	0.7	718	6.1	0.003 576	0.752	1.5	0.49	Eq. (5)
$\phi = 0.625$	0.6	457	5.3	0.002 241	0.726	1.5	0.50	Eq. (5)
$\phi = 0.5$	0.5	213	4.5	0.001 025	0.691	1.5	0.52	Eq. (5)
Nonreactive	1.1	1093	7.1	0.005 609	0.780	1.5	0.47	0
A	1.1	213	4.5	0.001 025	0.691	1.5	0.52	Eq. (5)
B	1.1	1093	4.5	0.001 025	0.691	1.5	0.52	Eq. (5)
C	1.1	1093	7.1	0.001 025	0.780	1.5	0.52	Eq. (5)
D	1.1	1093	7.1	0.005 609	0.780	1.5	0.52	Eq. (5)

reference Reynolds number Re_0 , Prandtl number Pr , and the Lewis number Le are defined as

$$\text{Re}_0 = \frac{\rho_0 u_0 l_0}{\mu_0}, \quad \text{Pr} = \frac{\mu_0 c_{p,0}}{\lambda_0}, \quad \text{Le} = \frac{\lambda_0}{\rho_0 D_0 c_{p,0}}. \quad (7)$$

The reference velocity u_0 is set to the laminar burning velocity S_L . The reference length l_0 is defined as $\approx 250\delta_{\text{th,st}}$, with $\delta_{\text{th,st}}$ being the initial thermal laminar flame thickness for the stoichiometric mixture. The reference speed of sound is defined as $a_0 = \sqrt{\gamma R_s T_0}$, where $\gamma = c_{p,0}/c_{v,0}$ is the heat capacity ratio and R_s is the specific gas constant. With this, a reference Mach number $\text{Ma}_0 = u_0/a_0$ can be defined. Both Ma_0 and Re_0 are functions of $u_0 = S_L$ and therefore dependent on flame properties. The shock Mach number is defined as $M_s = V_s/a$, where V_s is the velocity of the shock wave and $a = \sqrt{\gamma R_s T}$ is the local speed of sound. Another possible definition of the Reynolds number involves the usage of the velocity jump Δv induced by the shock on the flame surface. The difficulty in this definition lies in the fact that the velocity jump is dependent on the equivalence ratio and changes for shock and reshock. In addition, the velocity jump for the reshock can be difficult to determine analytically and is therefore not a suitable base for comparison. The reference Mach number Ma_0 can be interpreted as a dimensionless flame speed, since $\text{Ma}_0 = S_L/a_0$ and therefore a measure for the reactivity of the flame.

A low-storage 3rd order explicit Runge–Kutta scheme²⁵ is utilized for temporal discretization. The spatial derivatives of all

convective terms are calculated with the 5th order WENO-5 method by Jiang and Shu,²⁶ using the scalar Lax–Friedrichs flux splitting procedure described by Shu.²⁷ The scheme provides minimal-dissipation shock-capturing capabilities without numerical oscillations for the investigated cases. In order to assess the shock-capturing capabilities of the scheme in a reactive case, the 1D simulation results of a $\text{Ma}_s = 1.5$ shock wave interacting with a $\phi = 1.0$ flame (Table I) are shown in Fig. 2. At the beginning of the simulation, the shock is being initialized as a sharp discontinuity and then slightly smoothed by the WENO-5 scheme, which can resolve the shock within 2–3 nodes. The left column of Fig. 2 shows the normalized density and normalized temperature profiles before the shock interacts with the flame. Note that the normalized temperature is $T^* = 0$ in the unshocked and unburned part of the gas ($T = T_0$) and $T^* = 1$ in the unshocked and burned part of the gas ($T = T_{\text{ad}}$). In the right column of Fig. 2, the shock has passed the flame. The shock remains resolved sharply before and after the flame interaction and no spurious oscillations are visible. Note that the analytical solution does not take the flame into account, which causes an offset in the shock position between numerical and analytical solution after the flame has been passed.

III. SIMULATION SETUP

Figure 3 shows a schematic of the simulation domain, consisting of a rectangular channel divided into areas of unburned and burned gas by a statistically planar flame. At $x = 0$ a modified Navier–Stokes

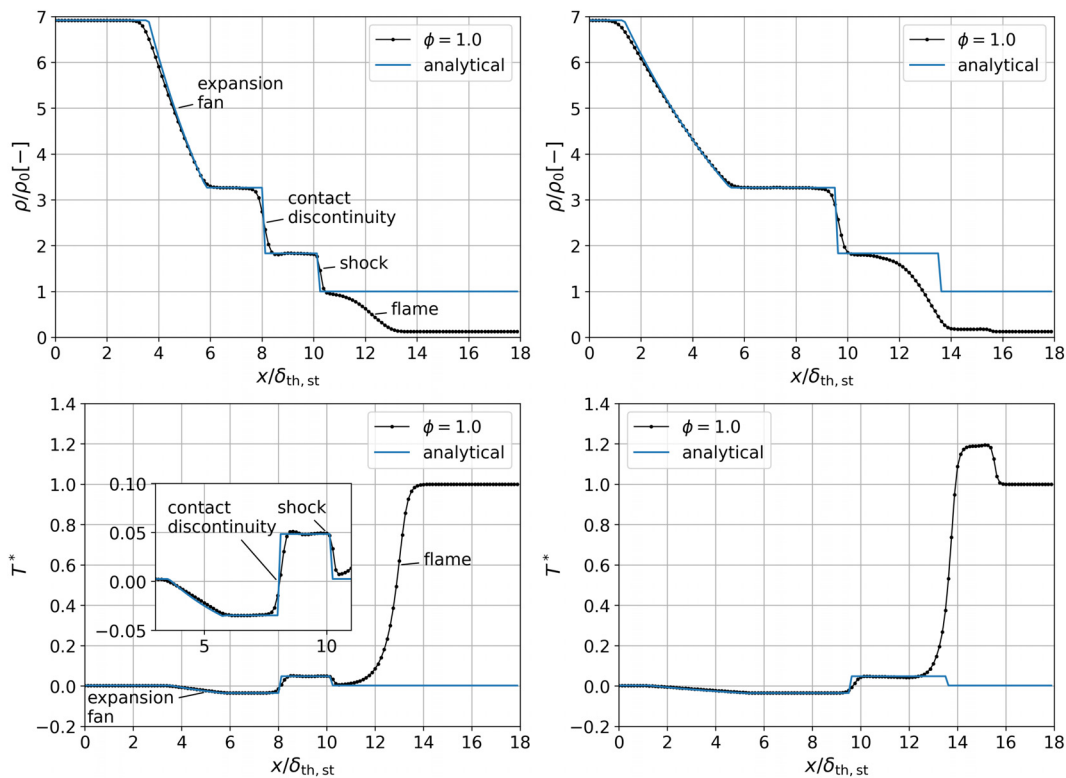


FIG. 2. Comparison of the numerical and analytical reactive shock-tube solution for $\phi = 1.0$ and $\text{Ma}_s = 1.5$. Normalized density (top) and normalized temperature (bottom) with $T^* = (T - T_0)/(T_{\text{ad}} - T_0)$ before (left column) and after (right column) shock-flame interaction.

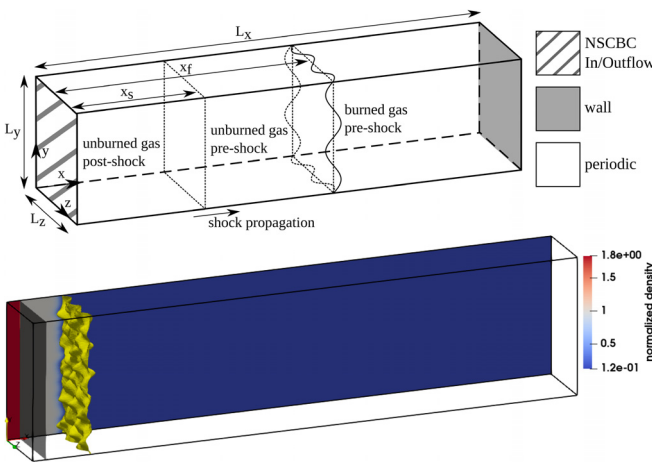


FIG. 3. Top: Setup schematic and boundary conditions with shock propagating from left to right and statistically planar flame. Bottom: 3D view and normalized density slice of initial case setup for $\phi = 1.0$. Flame and shock wave are represented by iso-surfaces of $c = 0.5$ (yellow) and $\rho/\rho_0 = 1.4$ (gray), respectively.

characteristic boundary condition (NSCBC) is implemented, allowing for both outflow and inflow of fluid.²⁸ An adiabatic wall boundary condition is applied at $x = L_x$, to enable the reflection of incoming shock waves. The boundary conditions in y and z -direction are periodic. At nonperiodic boundaries, a switch to an 8th-order central scheme is made. The stencil is then reduced stepwise down to second order and finally to a one-sided 2nd order scheme, as the boundary is approached.

An algorithm proposed by Tritschler *et al.*²⁹ is implemented to produce a well-defined initial disturbance of the flame surface. All presented cases are initialized with the flame disturbance field shown in Fig. 4, where the color represents the displacement in x -direction of the statistically planar flame surface. The displacement values are derived from a base oscillation with a wavenumber of $10\pi/L_y$ and superimposed with multi-wavenumber oscillations of small

amplitudes to enable a quasi-stochastic disturbance of the flame front. As visible in Fig. 4 (left) the wavelength of the base oscillation is much larger than $\delta_{th,st}$ and therefore well-resolved. The perturbations will not change significantly before the first shock interaction, as the time until shock interaction is very small ($t \times S_{L,st}/\delta_{th,st} = 0.025 \ll 1$). Figure 4 (right) shows the replanarization of the distorted flame surface in a hypothetical case without shock interaction. A sharp decline is visible at the beginning of the simulation as the smallest perturbations are smoothed due to numerical diffusion. At later times, the flame surface decreases slightly due to physical diffusion.

The grid sensitivity of the instability growth is shown alongside predictions of the Mikaelian model³⁰ in Fig. 5. In a nonreactive context, this model can be used to assess the growth of the mixing layer width. The model is applied to the $\phi = 1.0$ and the nonreactive case, where δ_m scales linearly ($\delta_m \sim t$) immediately after the shock interaction before transitioning at $t = t_m$ to nonlinear behavior ($\delta_m \sim t^{\theta_m}$). According to the model, the mixing layer width δ_m in the linear regime and nonlinear regime can be approximated as

$$\delta_{m,lin}(t) = \delta_{m,0} + 2\alpha_m A_{atw} \Delta v t, \quad \text{for } t \leq t_m, \quad (8a)$$

$$\delta_{m,\theta}(t) = \delta_{m,lin}(t = t_m) \left(1 + \frac{2\alpha_m A_{atw} \Delta v}{\delta_{m,lin}(t = t_m) \theta_m} (t - t_m) \right)^{\theta_m}, \\ \text{for } t \geq t_m. \quad (8b)$$

The transition time is approximated using $t_m \approx \delta_{m,0} \beta_m / \Delta v$, where $\delta_{m,0}$ is the mixing width at the start of the shock-flame interaction, Δv is the velocity jump at the mixing interface caused by the shock and $\beta_m = 6$ is a nondimensional constant. For the first shock interaction, Δv equals the postshock velocity $u_s = 124 S_L$, which can be calculated using the following nondimensional shock relation:

$$\frac{u_s}{S_L} = \frac{1 + \frac{\gamma - 1}{\gamma + 1} (Ma_s^2 - 1)}{Ma_s^2} \left(1 - \frac{Ma_s}{Ma_0} \right) + \frac{Ma_s}{Ma_0}. \quad (9)$$

Equation (9) is derived from the normal shock relations³¹ using $u_0 = S_L$ as the preshock velocity, T_0 as the preshock temperature and $V_s/S_L = Ma_s/Ma_0$. The growth parameters α_m and θ_m are

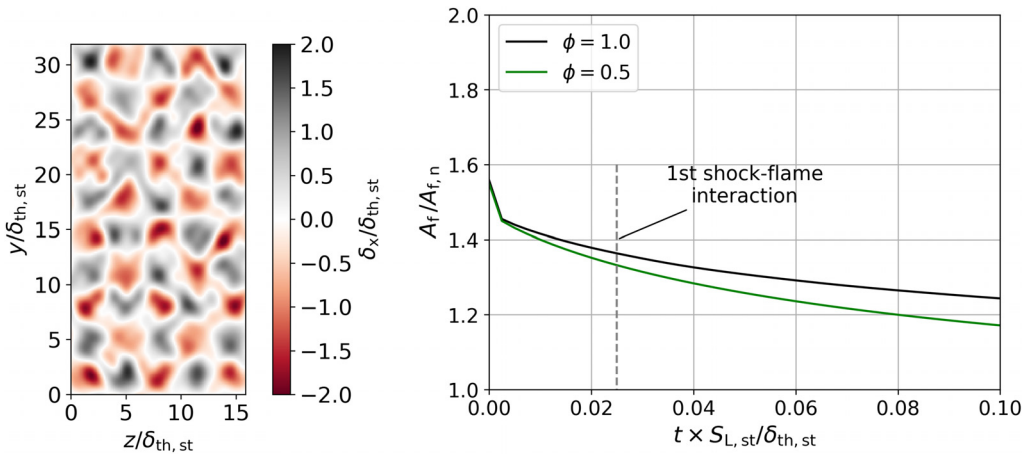


FIG. 4. Left: Normalized distortion $\delta_x/\delta_{th,st}$ of the statistically planar flame front. Right: Development of the disturbed flame surface in a hypothetical case without shock interaction for $\phi = 1.0$ and $\phi = 0.5$.

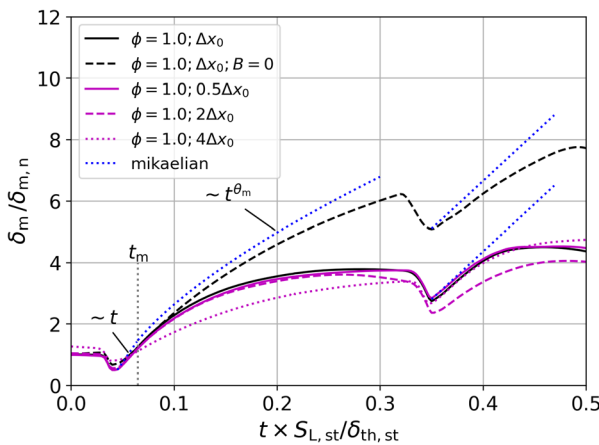


FIG. 5. Normalized mixing width over time for $\phi = 1.0$ and nonreactive gas mixture ($B = 0$) at different grid resolutions. Comparison with model predictions of the normalized mixing width.

approximated as $\alpha_m \approx 0.139$ and $\theta_m \approx 0.636$, using the following equations from Dimonte and Schneider:³²

$$\alpha_m \approx 0.07(1 + [(1 + A_{atw})/(1 - A_{atw})]^{0.33}), \quad (10a)$$

$$\theta_m \approx 0.25(1 + [(1 + A_{atw})/(1 - A_{atw})]^{0.21}), \quad (10b)$$

where the Atwood number $A_{atw} = (\rho_{ub} - \rho_b)/(\rho_{ub} + \rho_b) = 0.78$ describes a ratio of the burned (ρ_b) and unburned (ρ_{ub}) gas density. In the literature,^{33,34} typical values for the growth parameter θ_m have been shown to be between 0.213 and 0.666. Using the values above, the growth rate in the linear regime $\dot{\delta}_{m,lin} = 2\alpha_m A_{atw} \Delta v$ can be calculated as $\dot{\delta}_{m,lin} = 26.9 S_L$. A perfect fit of the model and the simulation results is not expected, since the transition time t_m and Eqs. (10a) and (10b) are approximations (see Mikaelian³⁰ for details). Nevertheless, the comparison emphasizes the similarities and differences between the reactive and the nonreactive case in terms of mixing width growth. Directly after the shock flame interaction, the mixing width scales linearly for both cases. After transitioning to the power law, the differences

between both cases become apparent, as the mixing width growth diminishes quickly for the reactive case. Decreasing the grid resolution (cases $2\Delta x_0$ and $4\Delta x_0$) causes an underestimation of the mixing width, since small perturbations can no longer be resolved. The fine ($0.5\Delta x_0$) and the base grid (Δx_0) follow the linear trend of the model by Mikaelian (“Mikaelian” in Fig. 5)³⁰ well and are in close agreement with each other during the nonlinear portion of the shock flame interaction. Hence, the results analyzed in the following can be considered as grid-convergent.

Equation (8a) also provides an explanation for the effect of shock Mach number variations as shown in Fig. 6. Increasing Ma_s leads to an increase in the velocity jump Δv which directly increases the initial growth rate of the mixing width. Comparing the mixing width growth between $\phi = 0.5$ and $\phi = 1.0$ reveals a much stronger nonlinear behavior for $\phi = 1.0$, whereas the growth is mostly linear for $\phi = 0.5$. This is caused by the increased reactivity in the stoichiometric case and will be further discussed in Sec. IV, where a detailed analysis of the effects of shock and reshock on the flame brush will be given.

The simulation parameters of the cases investigated in this work are listed in Table I. The two main cases are based on a H₂/air-gas mixture at an equivalence ratio of $\phi = 0.5$ (lean case) and $\phi = 1$ (stoichiometric case). Based on the setup of $\phi = 0.5$, the parameter variations A–D are performed, where Le , Re_0 , τ_h , and Ma_0 are successively changed to the parameters corresponding to the $\phi = 1$ case. Additionally, a nonreactive variation of the stoichiometric case is presented, where the pre-exponential factor is set to $B = 0$, hence deactivating the chemical source term $\dot{\omega} = 0$ [Eq. (5)]. For all cases, the shock Mach number is set to $Ma_s = 1.5$. The setup values for $\phi = 0.5$ and $\phi = 1$ are calculated using the Cantera software³⁵ and the GRI-MECH 3.0 database at $T_0 = 298.15\text{ K}$ and $p_0 = 1\text{ bar}$. The laminar flame speed S_L is calculated from Cantera to be 2.27 m/s for $\phi = 1.0$ and 0.385 m/s for $\phi = 0.5$. The pre-exponential factor B is calculated within a separate preprocessing step in SENGA, using the input parameters from Table I, so that the corresponding S_L is achieved. The simplest approach when calculating the Lewis number [Eq. (7)] for a gas mixture is to use the mass diffusion coefficient of the deficient reactant. For a lean mixture ($\phi < 1$) H₂ is the deficient reactant and for a fuel-rich mixture ($\phi > 1$) O₂ is the deficient reactant. In the limit

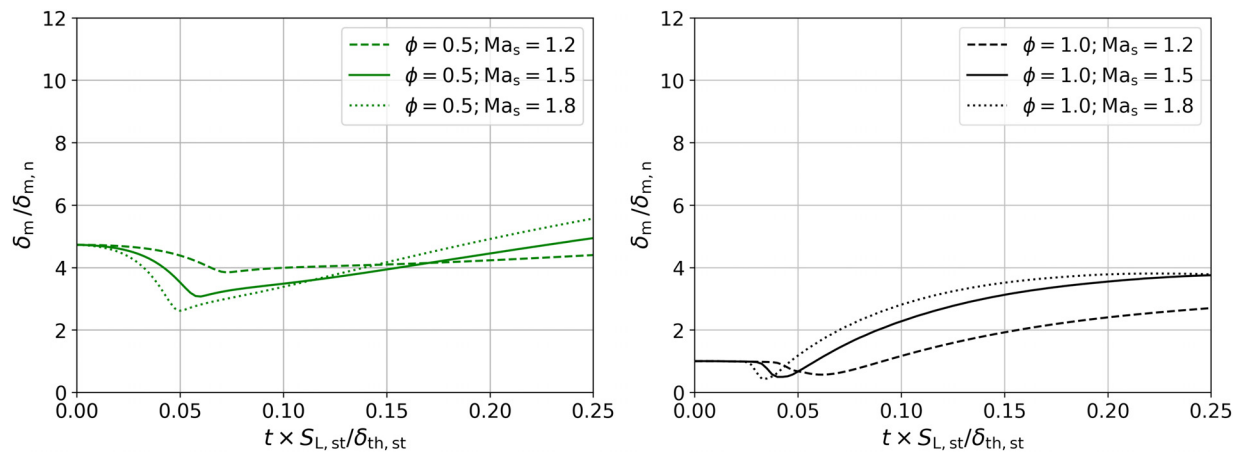


FIG. 6. Normalized mixing width over time for $\phi = 0.5$ (left) and $\phi = 1.0$ (right). Comparison of a shock-flame interaction at Mach numbers 1.2, 1.5, and 1.8.

of ($\phi \ll 1$), the H₂-Lewis number approaches $Le_{H_2} \approx 0.3$ and for ($\phi \gg 1$) the O₂-Lewis number approaches $Le_{O_2} \approx 2.1$. To avoid a jump at $\phi = 1$, an effective (also known as reduced) Lewis number Le_{eff} is defined, which provides a smooth transition between Le_{H_2} and Le_{O_2} over the whole range of ϕ . The following model for calculating Le_{eff} is taken from Bechtold and Matalon,³⁶ with Le_{H_2} and Le_{O_2} being provided by Cantera,

$$Le_{\text{eff}} = 1 + \frac{(Le_{H_2} - 1) + (Le_{O_2} - 1)A_{\text{Le}}}{1 + A_{\text{Le}}}. \quad (11)$$

The factor A_{Le} is defined by $A_{\text{Le}} = 1 + \beta_z(\tilde{\phi} - 1)$ with $\tilde{\phi} = \max(1/\phi, \phi)$. For the sake of simplicity, the subsequent discussion (including Table I) will refer to the effective Lewis number only as Lewis number or Le. Another approach for calculating an effective diffusivity, suitable for turbulent mixing of reactive species, is presented by O'Brien.³⁷

In Sec. IV the evolutions of the normalized flame surface area $A_f/A_{f,n}$ and the normalized mixing width $\delta_m/\delta_{m,n}$ are examined. As normalization constants $A_{f,n}$ and $\delta_{m,n}$, the cross section of the shock tube $L_y \times L_z$ and the initial mixing width for $\phi = 1.0$ at $t = 0$ are chosen. Equation (12) shows the equations used to calculate A_f ³⁸ and δ_m ³⁹ from the simulation data, where $\langle \cdot \rangle$ indicates averaging in the yz -plane. The definition of A_f , which represents the total flame surface area evaluated over the entire simulation domain, is based on the volume integral of the generalized flame surface density (FSD),⁴⁰

$$A_f = \iiint_V |\nabla c| dV, \quad (12a)$$

$$\langle c \rangle = \frac{1}{L_y L_z} \iint c dy dz, \quad (12b)$$

$$\delta_m = \int_0^{L_x} 4\langle c \rangle (1 - \langle c \rangle) dx. \quad (12c)$$

In the context of LES subgrid model closure, evaluating $A_f/A_{f,n}$ and $\delta_m/\delta_{m,n}$ can be of pivotal importance, since they can be related to the closure of the reaction rate term and the convective term.

All length dimensions are normalized by the thermal laminar flame thickness $\delta_{\text{th,st}}$ at $\phi = 1$. The dimensions of the domain are $L_x \times L_y \times L_z = 128\delta_{\text{th,st}} \times 32\delta_{\text{th,st}} \times 16\delta_{\text{th,st}}$ uniformly discretized by $1024 \times 256 \times 128$ grid points. The shock and flame are initialized at $x_s = 3.125\delta_{\text{th,st}}$ and $x_f = 12.5\delta_{\text{th,st}}$, respectively. The initial thermal laminar flame thickness of the lean case is $\delta_{\text{th,le}} \approx 8\delta_{\text{th,st}}$ with $\delta_{\text{th}} = 1/\max|\nabla T^*|$.

IV. RESULTS

Figure 7 shows density slices in the xy -plane at different times for $\phi = 1.0$ and $\phi = 0.5$. The density is normalized using the unburned and unshocked reference density ρ_0 . The shock is visible as a discontinuity in ρ , increasing ρ/ρ_0 on each passage through the shock tube. The simulation ends at $t \times S_{\text{L,st}}/\delta_{\text{th,st}} = 1$. The time steps $t_a, t_b, t_c, t_d \times S_{\text{L,st}}/\delta_{\text{th,st}} = 0.2, 0.4, 0.6, 0.8$ show different stages of the RMI development. Sharp⁴¹ describes four different stages of development for the phenomenologically similar RTI:

- Initial linear growth of flame perturbations.
- Formation of fresh gas cusps.
- Development of wrinkled structures.

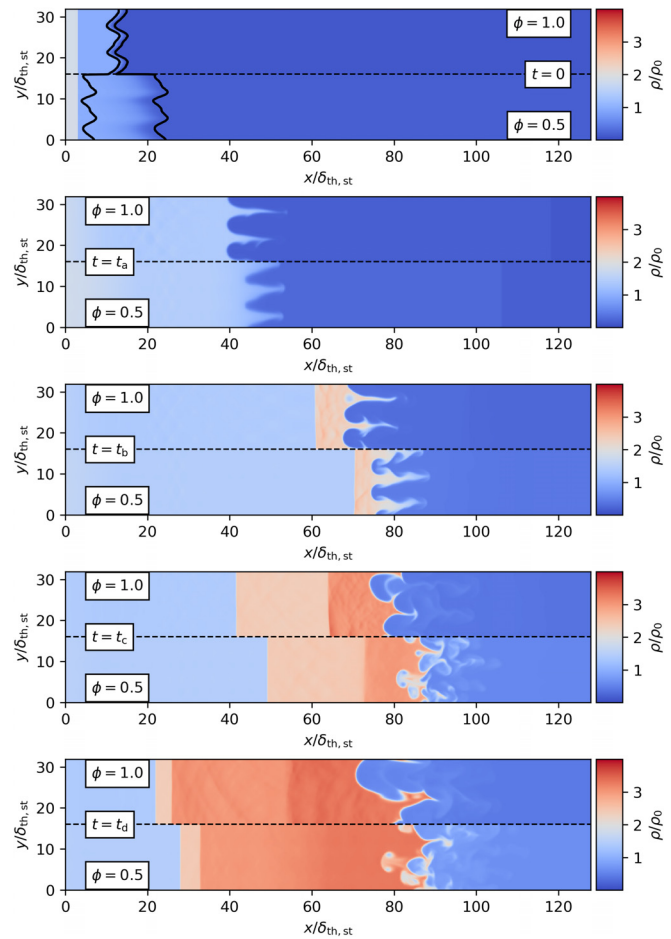


FIG. 7. Density slices ($z = L_z/2$) of the shock-flame interaction for $\phi = 1.0$ and $\phi = 0.5$. Timesteps $t_a, t_b, t_c, t_d \times S_{\text{L,st}}/\delta_{\text{th,st}} = 0.2, 0.4, 0.6, 0.8$. Isocontours of the reaction progress variable ($c = 0.02$ and $c = 0.98$) show the difference in flame thickness at $t = 0$.

- Break up of distinct cusps and creation of a chaotic mixing layer.

At t_a , the shock wave, which is propagating from left to right, has already interacted with the flame surface for the first time, causing the creation of distinct fresh gas cusps, which extend into the burned gas mixture. The influence of the initial displacement (Fig. 4) can still be identified as the flame cusps are inverted and further disturbed by the RMI (Fig. 1). In the context of premixed flames interacting with pressure gradients, a similar cusp-creation effect has been observed by Lipatnikov *et al.*⁴² and Poludnenko.⁴³ The increased reactivity at $\phi = 1.0$ causes a transverse burnout of the fresh gas cusps, leading to the creation of regions of strong negative curvature (sharp edges). At t_b , the shock has been reflected from the back wall ($x = L_x$) and has interacted with the flame surface a second time (reshock). While the maxima of the initial disturbance can still be identified at this stage of the RMI, the distortions are increased further and small-scale wrinkled structures emerge on the flame surface. The shock wave is partially reflected from the flame surface at t_b . This partial reflection interacts

with the flame shortly before t_c , causing further wrinkling of the flame brush and the creation of a mixing region of burned and unburned gas. At this stage, the influence of the equivalence ratio ϕ becomes especially apparent as locally emerging small-scale wrinkles are burned out for $\phi = 1.0$, leaving only larger-scale structures with regions of high negative flame curvature in between. The reduction of perturbation growth due to diffusion is an important mechanism of reactive RMI and is discussed and evaluated by Attal and Ramaprabhu.⁴⁴ An effect of similar nature (decreasing the wrinkling) caused by molecular diffusion on a reactive flame surface is discussed by Yu and Lipatnikov.⁴⁵ The last slice at t_d shows the development of the RMI toward the end of the simulations. The overall structure of the flame and the differences between $\phi = 1.0$ and $\phi = 0.5$ do not change significantly to the state discussed at t_c . At this late stage, the flame surface area reduces a little, due to diffusion effects and the interaction and merging of neighboring wrinkled structures. In the burned gas region ($T = T_{ad}$), the velocity V_s of a shock wave traveling at Mach number M_{as} is defined by $V_s = M_{as} \sqrt{\gamma R_s T_{ad}}$. Since T_{ad} is higher for $\phi = 1.0$ than for $\phi = 0.5$, the shock waves propagate at different velocities inside the burned gas mixture, creating a visible offset in the shock position between both cases. The development of the 3D flame brush is shown in Fig. 8. The flame surface is represented by a yellow isosurface at $c = 0.5$. This visualization further highlights the influence of the equivalence ratio on the flame brush development, which becomes particularly apparent after the reshock. From $t = t_b$ to $t = t_d$ large flame cusps are starting to develop and grow for $\phi = 1.0$, whereas for $\phi = 0.5$, the developing wrinkled structures are found to be of a much smaller scale.

A. Flame surface area and mixing width analysis

In order to further assess the temporal development of the RMI, the evolution of the normalized flame surface area $A_f/A_{f,n}$ and the normalized mixing width $\delta_m/\delta_{m,n}$ are analyzed in Fig. 9. An additional nonreactive ($\dot{\omega} = 0$) variation of $\phi = 1.0$ is analyzed by setting $B = 0$ in Eq. (5). Generally, two different phases in the evolution of $A_f/A_{f,n}$ can be distinguished. The first phase is characterized by the initial growth during and shortly after interaction with the shock wave, caused by the production of baroclinic torque on the flame surface (see Sec. IV B for a more detailed discussion on the influence of baroclinic torque and enstrophy). The amount of baroclinic torque produced is dependent on the magnitude of the pressure gradient ∇p across the shock, the density gradient $\nabla \rho$ across the flame, and the misalignment of shock wave and flame surface. Since cases $\phi = 1.0$ and $\phi = 0.5$ are set up using the same initial flame disturbance and initial shock Mach number ($M_{as} = 1.5$) the only influencing factor left to explain the differences in the initial development of $A_f/A_{f,n}$ is $\nabla \rho$. Increasing the equivalence ratio from $\phi = 0.5$ to $\phi = 1.0$ increases $\nabla \rho$ by significantly reducing the flame thickness and increasing T_{ad} and therefore increasing the density difference between the burned and unburned sides of the flame. The flame thickness δ_f (Fig. 9) is defined by $\delta_f = V_f/A_f$, where the flame volume V_f is calculated by summation of all grid points with $0.01 \leq c \leq 0.99$. The increase in $\nabla \rho$ causes a higher baroclinic torque production and subsequently a steeper initial increase and higher maximum value in $A_f/A_{f,n}$ for $\phi = 1.0$ compared with $\phi = 0.5$. At reshock, the development of $A_f/A_{f,n}$ shows different behaviors. The rise of $A_f/A_{f,n}$ after the reshock is similar in both cases (and the nonreactive case) until

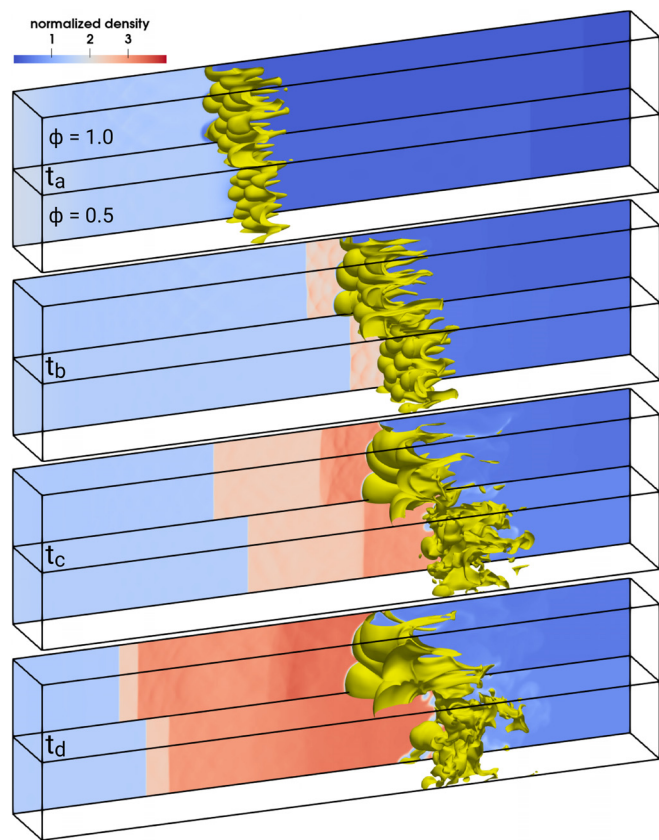


FIG. 8. 3D view and normalized density slice of the shock-flame interaction for $\phi = 1.0$ (top half) and $\phi = 0.5$ (bottom half). Timesteps $t_a, t_b, t_c, t_d \times S_{L,st}/\delta_{th,st} = 0.2, 0.4, 0.6, 0.8$. The flame is represented by a yellow isosurface at $c = 0.5$.

$\phi = 1.0$ reaches a peak and decreases rapidly, while $\phi = 0.5$ continues to rise, surpassing the stoichiometric case. The differences to the first shock-flame interaction can be attributed to two reasons. First, at the reshock, the flame thickness of $\phi = 0.5$ is reduced significantly (Fig. 9), as the shock wave increases the pressure and compresses the flame, increasing $\nabla \rho$ for this case. Second, as visible in Fig. 7 at t_b , the development of wrinkled structures on the flame surface is a key contributing factor on the overall growth of the flame surface area. As already mentioned in the discussion of Fig. 7, the increased reaction rate at $\phi = 1.0$ locally burns out the wrinkled structures, which reduces the achievable surface area growth.

The phase of growth after each shock-flame interaction is followed by a second phase, where $A_f/A_{f,n}$ reaches a peak value before decreasing again. This decrease can be caused by several factors, including molecular diffusion, structures merging and thereby removing surface area and the already mentioned reactive burnout of emerging wrinkled structures. The main influencing factor in this phase of $A_f/A_{f,n}$ development is the reaction rate of the gas mixture, which is shown by comparing the results with the nonreactive case at $\phi = 1.0$. Deactivating the chemical reaction prevents the decrease in $A_f/A_{f,n}$ after the first shock interaction and reduces it significantly for the reshock. The nonreactive case reaches similar values as the lean ϕ

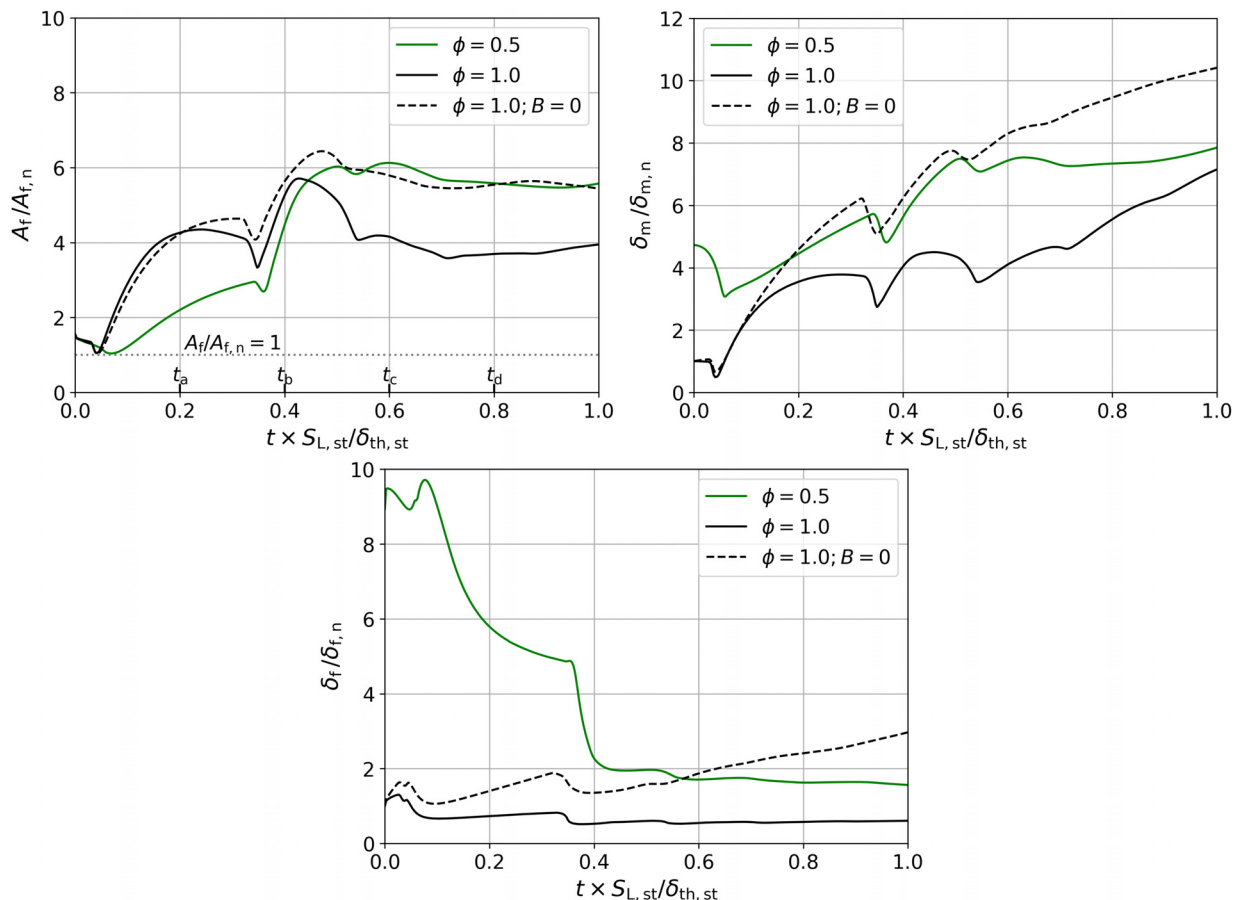


FIG. 9. Normalized flame surface area (top left), normalized mixing width (top right), and normalized flame thickness (bottom) over time for $\phi = 0.5$, $\phi = 1.0$ and nonreactive gas mixture.

$= 0.5$ case, which indicates that the latter case shows elements of passive scalar mixing (this will be further investigated in Sec. IV C). Another observation is the short drop to $A_f/A_{f,n} = 1$ during the first shock interaction, which is caused by the phase reversal effect explained in Fig. 1 ($A_f/A_{f,n} = 1$ indicates a planar flame). The other drop, visible directly at the beginning of the reshock, is not related to the phase reversal effect, but is rather caused by the shock interacting with the leading flame structures first, before interacting with the rest of the flame. The overall rise in the flame area due to the effects of the RMI is quite significant in both cases, with a maximum increase in around 400%, compared to their values at $t = 0$.

Figure 9 (right) shows the development of the normalized mixing width $\delta_m/\delta_{m,n}$ [Eq. (12c)] over time. In a nonreactive context, the mixing width represents the size of the mixing layer of heavy and light fluids, developing over time due to the RMI. While this explanation is also valid in the context of a reactive gas, there is an additional contribution to δ_m from the flame thickness itself. This means that an unmixed [i.e., no (turbulent) mixing layer of unburned and burned gas] reactive gas will show a nonzero mixing width due to the thickness of the flame. This can be seen at $t = 0$, where the initial value of $\delta_m/\delta_{m,n}$ is about 4 times higher for $\phi = 0.5$ than for $\phi = 1.0$, due to

the increased flame thickness of the lean case. While overall the $\delta_m/\delta_{m,n}$ ratio is increasing over time due to the mixing effect of the RMI, the overlapping effect of flame thickness reduction due to the shock interaction causing short periods of decreasing mixing width. In the last phase of the simulation for $\phi = 1.0$, large cusps of burned gas extend into the unburned mixture (Fig. 7, t_d) causing the mixing width to grow. This effect is less pronounced for $\phi = 0.5$ because of the lower reactivity, but balanced out by the higher flame thickness and increased wrinkling and mixing due to the RMI. The nonreactive case achieves the highest $\delta_m/\delta_{m,n}$ ratio, which can be attributed to an increase in wrinkling and mixing in the absence of reactive burnout. The absence of a reactive source term in the nonreactive case causes an increase in the interface thickness (nonreactive equivalent to the flame thickness) due to diffusion (Fig. 9). As indicated earlier, this effect also contributes to the growth of the mixing width.

In order to further analyze the influence of ϕ on the development of the flame surface area and mixing width, a parametric analysis is performed (cases A–D in Table I). Starting with the case settings for $\phi = 0.5$, the Lewis number (case A) and, subsequently, the reference Reynolds number (case B) are changed to the values used for $\phi = 1.0$. For both cases, this leads to a significant reduction of the flame

thickness (Fig. 10), causing a higher density gradient across the flame and higher production of baroclinic torque. As seen in Fig. 10, this increases the $A_f/A_{f,n}$ gradient at the first shock-flame interaction, and higher peak values are reached than for $\phi = 0.5$. For later times $A_f/A_{f,n}$ values in cases A and B decrease again to values close to $\phi = 0.5$, due to surface reduction from diffusive effects. Case C additionally increases T_{ad} (higher τ_h), which again leads to a larger density gradient across the flame and larger values of $A_f/A_{f,n}$. Cases A–C reduce the flame thickness and increase T_{ad} to the values for $\phi = 1.0$ and both effects aid the development of RMI. The last performed variation D increases the reference Mach number Ma_0 , which can be interpreted as a dimensionless flame speed ($Ma_0 = S_L/a_0$) and therefore increases the reactivity to values very close to $\phi = 1.0$. Now the already mentioned burnout effect becomes more significant and reduces the reachable $A_f/A_{f,n}$ values to the values seen for $\phi = 1.0$. No variation for the Prandtl number is performed as the numbers are already quite similar for both ϕ .

Analyzing the mixing width in Fig. 10 leads to similar conclusions as already discussed for Fig. 9. Again, the mixing width values are not only influenced by the mixing of heavy and light fluids at the interface but also by the changes in flame thickness. Although the interference of flame thickness and diffusion effects can make a

detailed assessment difficult, the increased baroclinic torque (due to the higher density gradient across the flame) essentially leads to more mixing as measured by the increase in $\delta_m/\delta_{m,n}$, while increasing the reactivity in case D reduces the mixing. Cases B–D show a similar behavior as $\phi = 1.0$ toward the end of the simulation, where $\delta_m/\delta_{m,n}$ keeps rising linearly.

Figure 11 shows a detailed view of the flame brush structure at time t_c and its transition from $\phi = 0.5$ to $\phi = 1.0$ via the cases A–D. Notable is the reduction in flame thickness from $\phi = 0.5$ to case B, leading to sharper defined structures. While the increased density gradient is less visible in case C, the change in reactivity from case C to D is clearly noticeable. The small wrinkled structures are burned out and only large bubble-like structures remain, which extend into the unburned mixture.

Since the Lewis number is significantly smaller than unity for $\phi = 0.5$, the flame might be more susceptible to thermodiffusive instabilities in addition to the effects of the RMI. For the variation case A, the Lewis number is increased to 1.1, while the other parameters correspond to the lean case. While this method does not allow to fully isolate the effects of RMI and thermodiffusive instabilities, it is supposed to give a general insight into how other instabilities overlay with the effects of the RMI. Increasing the Lewis number to 1.1 may

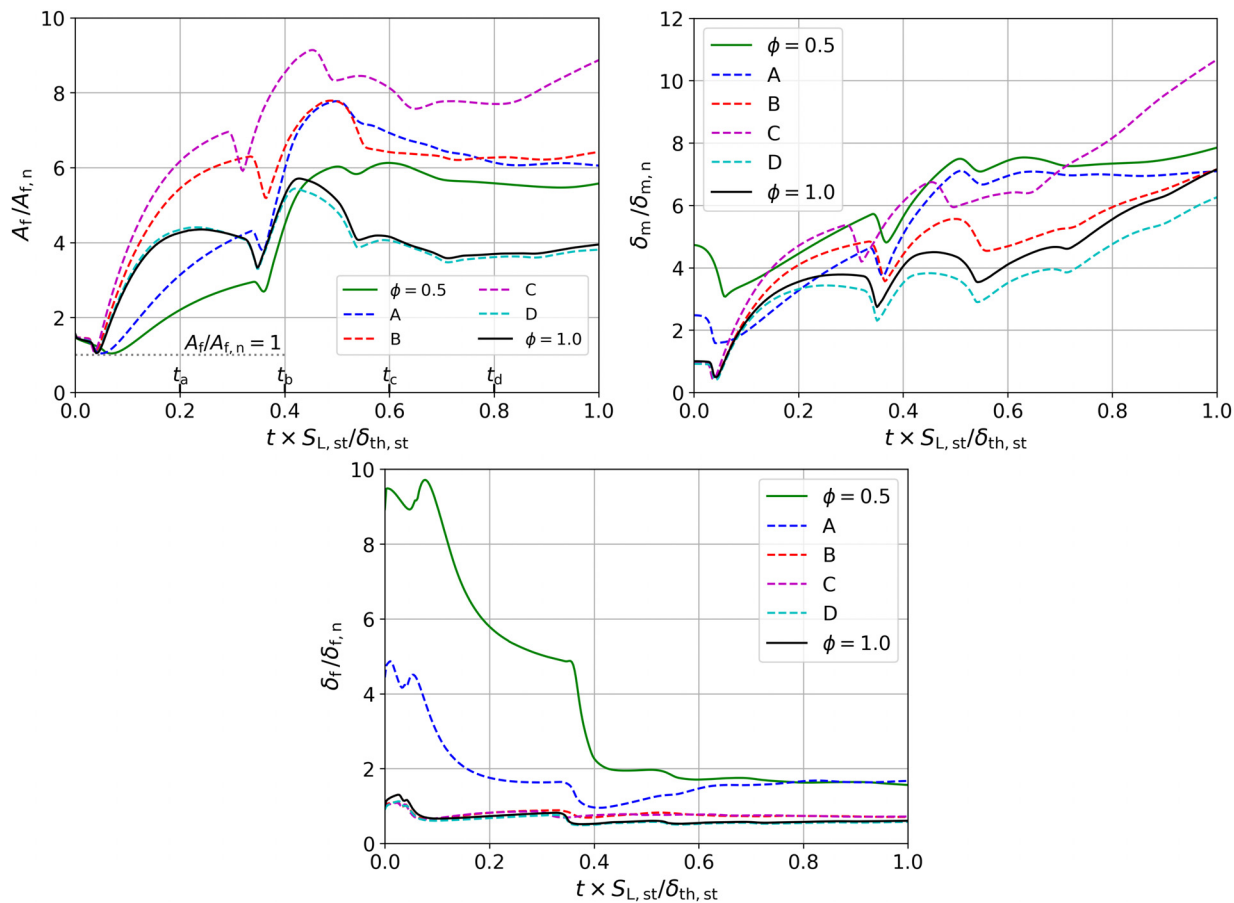


FIG. 10. Normalized flame surface area (left), normalized mixing width (right), and normalized flame thickness (bottom) over time for $\phi = 0.5$, $\phi = 1.0$ and cases A–D.

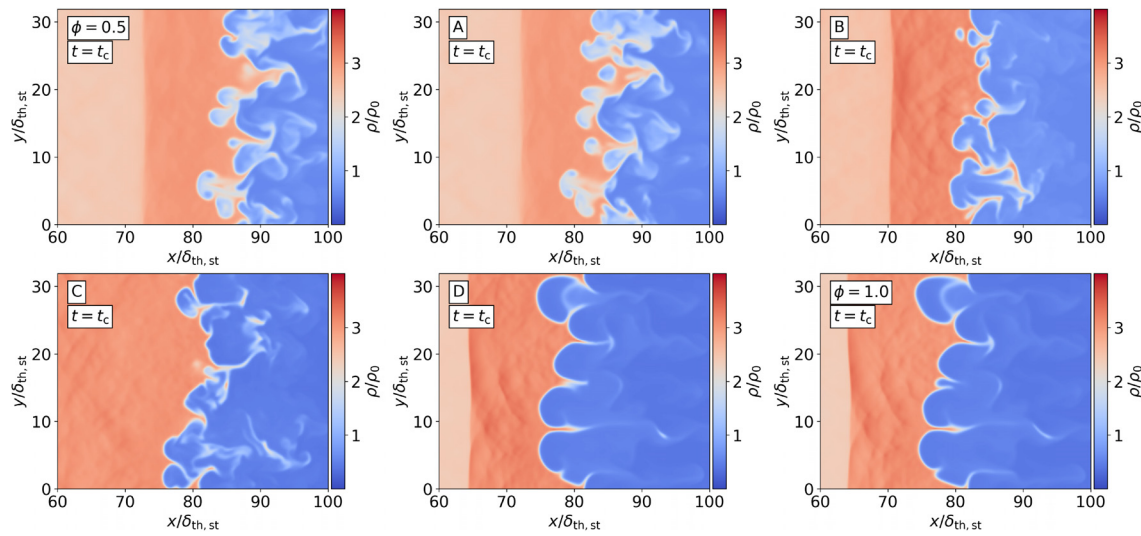


FIG. 11. Detailed view of density slice at $t = t_c$ for $\phi = 0.5$, $\phi = 1.0$ and cases A–D.

decrease the susceptibility of the flame toward thermodiffusive instabilities, but as shown in Fig. 10, it will severely increase the effects of the RMI due to the decrease in the flame thickness.

A numerical parametric analysis conducted by Bambauer, Hasslberger, and Klein⁴⁶ investigates the effect of M_{∞} and variations of the initial flame disturbance on the development of A_f and δ_m for a nonreactive case ($\dot{\omega} = 0$). It is shown that increasing M_{∞} leads to higher values of A_f and δ_m , since the amount of baroclinic torque produced at the flame surface is directly dependent on the shock pressure gradient. The initial flame disturbance can also have a great impact on the development of the flame surface and mixing, since each local maximum in the initial disturbance field (Fig. 4) acts as a source for the formation of fresh gas cusps. This can initially increase the flame surface area but also cause a loss, if the cusps interact and merge at later stages of the RMI.

B. Enstrophy analysis

The generation of vorticity due to baroclinic torque at the flame surface is the initiating mechanism for the RMI. The enstrophy $\Omega = \omega_i^2/2$ can be interpreted as a scalar energy equivalent of the vorticity $\omega_i = \varepsilon_{ijk}\partial u_k/\partial x_j$ and its transport equation is given as

$$\frac{\partial \Omega}{\partial t} + u_k \frac{\partial \Omega}{\partial x_k} = \underbrace{\omega_i \omega_k \frac{\partial u_i}{\partial x_k}}_{T_I} - \underbrace{\varepsilon_{ijk} \omega_i \frac{1}{\rho^2} \frac{\partial \rho}{\partial x_j} \frac{\partial \tau_{kl}}{\partial x_l}}_{T_{II}} + \underbrace{\frac{\varepsilon_{ijk} \omega_i}{\rho} \frac{\partial^2 \tau_{kl}}{\partial x_j \partial x_l}}_{T_{III}} \\ - 2 \underbrace{\frac{\partial u_k}{\partial x_k} \Omega}_{T_{IV}} + \underbrace{\varepsilon_{ijk} \frac{\omega_i}{\rho^2} \frac{\partial \rho}{\partial x_j} \frac{\partial p}{\partial x_k}}_{T_V}. \quad (13)$$

The terms on the right-hand side represent the changes in enstrophy due to vortex stretching (I), viscous torque (II), dissipation (III), dilatation (IV), and baroclinic torque (V). A thorough discussion of the individual enstrophy transport terms in the context of turbulent combustion can be found in Lipatnikov *et al.*⁴⁷ and Chakraborty

*et al.*⁴⁸ Figure 12 shows the volume integrals of the enstrophy transport terms for $\phi = 0.5$ and $\phi = 1.0$. Each peak in the baroclinic torque term (term V) represents a shock-flame interaction. During the first and second shock-flame interactions, the baroclinic torque dominates the overall enstrophy change, as indicated by the maximum reached peak height. At later times, terms I, III, and IV significantly gain in importance and should be included in the discussion. At the first interaction, the difference in flame thickness and adiabatic flame temperature leads to a higher peak in baroclinic torque for $\phi = 1.0$ than for $\phi = 0.5$. The situation is reversed at the reshock, where the decrease in flame thickness and build up of additional wrinkled structures on the flame surface support the production of baroclinic torque for $\phi = 0.5$. The third peak is caused by the interaction with the partially reflected shock wave shown in Fig. 7 at time t_c . As shown in Fig. 13, local areas of positive and negative baroclinic torque contributions can be present during the entire period of the shock-flame interaction. Since Fig. 12 shows volume integrals, the negative and positive contributions partially cancel out each other, leaving only the net contribution for the entire domain. In the case of the baroclinic torque, the net contribution is positive at the beginning of the shock-flame interaction, meaning it acts as a source of enstrophy, but this is followed by a short period of negative net contribution, where it acts as a sink. Similar behavior is seen for the dilatation term (term IV) at $\phi = 1.0$, where the positive peak during the shock interaction is followed by a decrease to negative values at later times. Another interesting observation is the similarity of the vortex stretching (term I) and dissipation (term III) terms, which act in opposite directions effectively canceling out each other (especially apparent for $\phi = 1.0$). Figure 13 shows the planar shock wave evolving into a complex-shaped shock pattern with multiple microreflections, as it is successively deflected and reflected when moving through the perturbed flame surface. After exiting the flame vicinity, the shock patterns merge into a planar shock again.

In order to assess the importance of the individual terms on the enstrophy development over time, the integral enstrophy budget is calculated for each term. This can be also interpreted as the

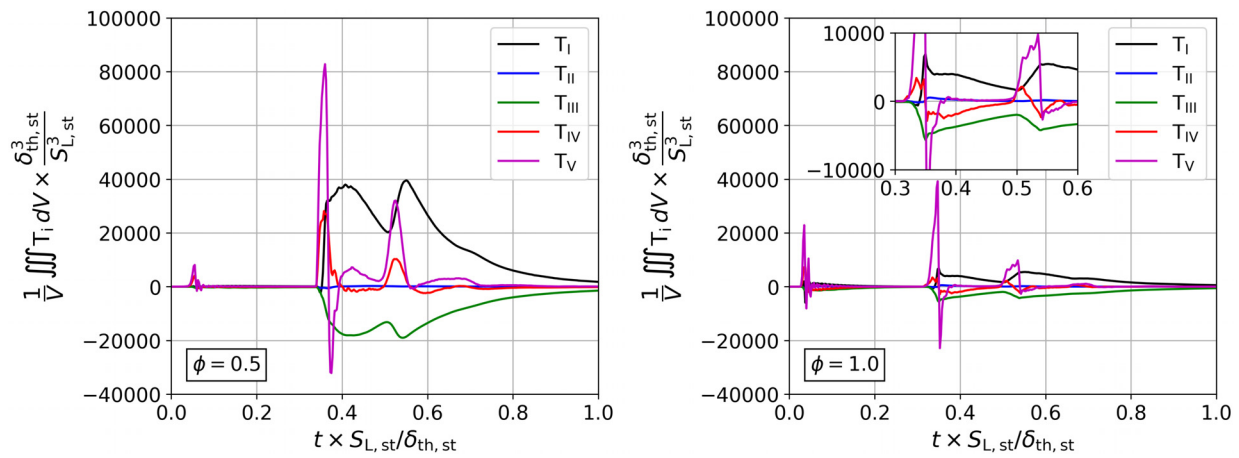


FIG. 12. Normalized volume integral (with $V = L_x L_y L_z$) of the instantaneous enstrophy transport terms for $\phi = 0.5$ (left) and $\phi = 1.0$ (right).

temporal development of the area integral below each graph in Fig. 12. The stacked plots in Fig. 14 show the percentage ratio of the integral enstrophy budget for each term to the total enstrophy budget T_{sum} over time. The moments of shock-flame interaction and therefore the spikes in baroclinic torque production are clearly visible in Fig. 14 for both cases, as term V is responsible for 50%–60% of the total integral enstrophy budget changes in these moments. After the peak in baroclinic torque, the vortex stretching term (term I) and dissipation term (term III) become significantly more important. Toward the end of the simulation, terms I and III account for about 75% of the total integral enstrophy budget

changes for $\phi = 0.5$ and about 65% budget changes for $\phi = 1.0$. As both terms act against each other (Fig. 12), term III reduces term I for $\phi = 0.5$ and cancels out term I for $\phi = 1.0$. A similar result is obtained by Cabot⁴⁹ for miscible 3D RT-simulations, where the baroclinic torque term is the dominant term in the initial stages of the RT instability but later the vortex stretching term becomes the dominant mechanism. For both cases, the dilatation term (term IV) takes a share of about 5%–20% throughout the whole simulation. While the influence of viscous torque (term II) can be neglected in the present cases, an influence of about 10% is reported by Liu *et al.*⁵⁰ for high shock Mach numbers.

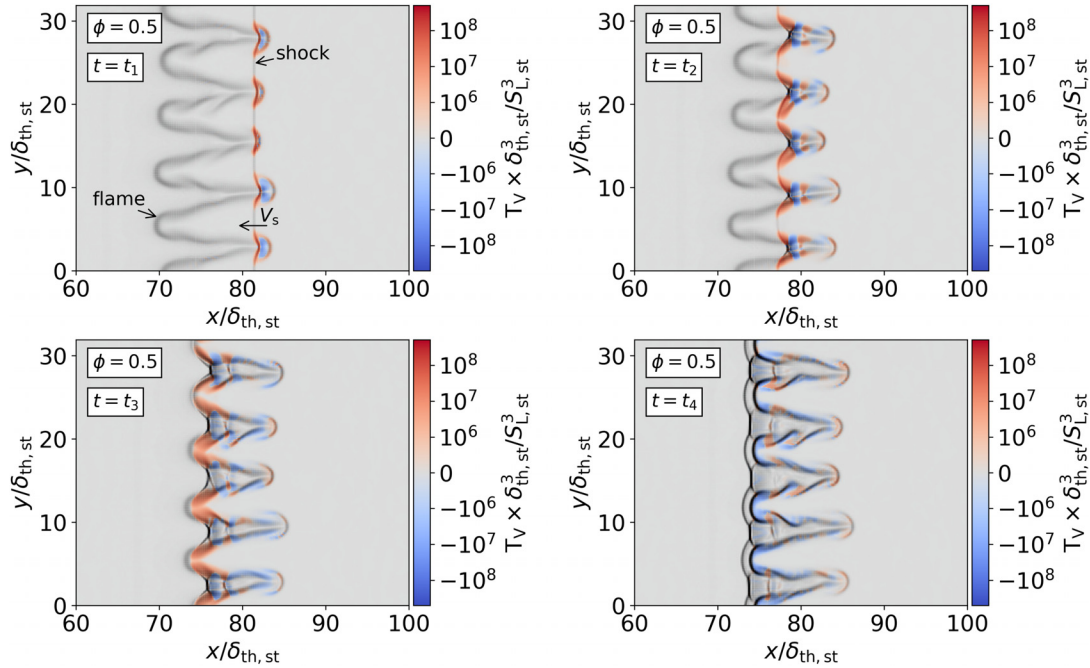


FIG. 13. Detailed view of baroclinic torque slice with numerical schlieren (in grayscale) at $t_1, t_2, t_3, t_4 \times S_{L, \text{st}} / \delta_{\text{th}, \text{st}} = 0.345, 0.355, 0.365, 0.375$ (during reshock) for $\phi = 0.5$.

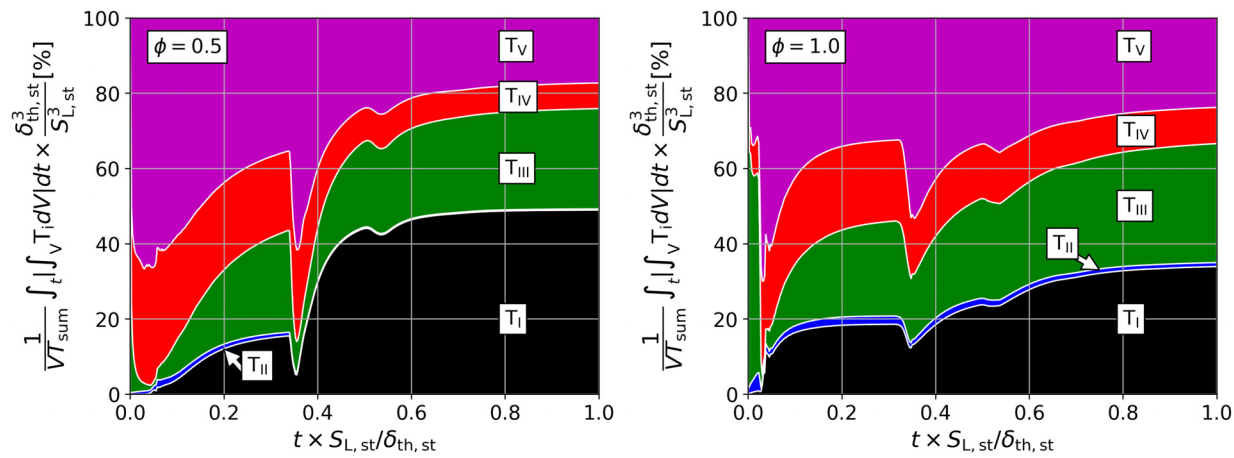


FIG. 14. Percentage share of the enstrophy transport terms on the sum of integral enstrophy budgets T_{sum} over time for $\phi = 0.5$ (left) and $\phi = 1.0$ (right).

To gain a better insight of the influence of the equivalence ratio ϕ on the development of the enstrophy terms, the development of terms I and V (the two dominant terms) is compared for cases A–D in Fig. 15. The effects of decreasing the flame thickness (mostly visible for case B) and increasing the adiabatic temperature (case C) all result in a significant increase in both terms. When the influence of an increased reaction rate is considered via case D, the values of the terms reduce significantly again to the values seen for $\phi = 1.0$ (Fig. 15).

C. Fractal analysis

A common approach for reaction rate closure in RANS and LES is to model the subgrid scale wrinkling factor $\Xi = A_T/A_\perp = \overline{|\nabla c|}/|\nabla \bar{c}|$ (overbar indicates RANS averaging or LES filtering) as a power-law function, where A_T is the turbulent flame area and A_\perp the projected flame area. If the filter width is chosen so that $A_\perp = A_{f,n} = L_y L_z$, then the normalized flame surface area in Fig. 9

can be also interpreted as a wrinkling factor Ξ . The power-law modeling results in the expression,^{51,52}

$$\Xi = (\eta_o/\eta_i)^{D_t-2}. \quad (14)$$

The outer and inner cutoff scales η_o and η_i are taken as the LES filter width Δ and a quantity that corresponds to the smallest occurring flame wrinkles,⁵³ respectively. For unity Lewis number the turbulent flame speed $S_T = \int_V (\dot{\omega}/\rho_{ub}) dV/A_\perp$ (a fundamental quantity for reaction rate closure) can be related to the wrinkling factor Ξ (strictly speaking for statistically planar flames) by invoking Damköhler's first hypothesis,⁵⁴

$$S_T/S_L = \Xi = A_T/A_\perp. \quad (15)$$

By explicitly filtering the present data, Ξ and the projected flame area A_\perp can be calculated.^{55,56} The standard definition of S_T assumes a constant unburned gas density ρ_{ub} . This assumption is not valid in the

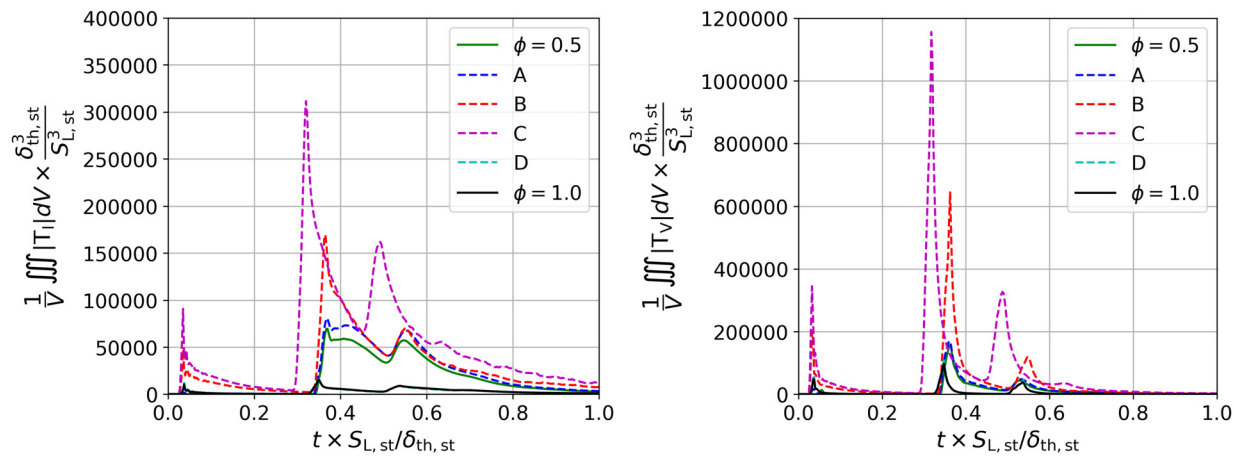


FIG. 15. Normalized volume integral (with absolute values) of the enstrophy transport terms I (left) and V (right) for $\phi = 0.5$, $\phi = 1.0$ and cases A–D. Note that the curves for D and $\phi = 1.0$ collapse.

present cases, since the shock wave causes a density jump as it passes the flame. The corrected unburned density is calculated from the (partially) burned state of the gas mix for $\phi = 1.0$ with $\rho_{ub} = \rho(1 + \tau_h c)$, which is valid when the thermodynamic pressure remains unchanged. While this approach provides very good results for $\phi = 1.0$, the approximation is not valid for $Le \ll 1$ ($\phi = 0.5$). For $\phi = 0.5$ the corrected unburned density can be approximated using the isentropic relation $\rho_{ub} = \rho_0(p/p_0)^{1/\gamma}$. In principle, the idea is to approximate a corrected unburned density from the (partially) burned state of the flame (using ρ and p). For an unshocked burned state, the unshocked unburned density is calculated. For a shocked burned state, the shocked unburned density is calculated. The key to both approaches is that no explicit shock treatment is necessary, since the shock effects are already included in the values of ρ and p . Deviations of the ratio $(S_T/S_L)/\Xi$ from unity specify the departure from Damköhler's hypothesis shown in Eq. (15). Figure 16 shows that for $\phi = 1.0$, the Damköhler hypothesis is met very well, with minor deviations during shock-flame interactions and after reshock. In comparison, the deviations are significantly higher for $\phi = 0.5$, since the Damköhler hypothesis is not valid for $Le \ll 1$ (see Chakraborty *et al.*⁵⁷).

The method of explicitly filtering the data also allows to calculate the fractal dimension D_f of the premixed flame. With the generalized flame surface density (FSD) $\Sigma_{gen} = |\nabla \bar{c}|$ defined by Boger *et al.*⁴⁰ and using Eq. (14) the following expression for Σ_{gen} is obtained:⁵⁸

$$\Sigma_{gen} = |\nabla \bar{c}|(\Delta/\eta_i)^{D_f - 2}. \quad (16)$$

Following the method described in detail by Chakraborty and Klein⁵⁵ and taking the volume average of Eq. (16), results in

$$\log(\langle \Sigma_{gen} \rangle / \langle |\nabla \bar{c}| \rangle) = (D_f - 2) \log(\Delta) - (D_f - 2) \log(\eta_i). \quad (17)$$

Equation (17) can be interpreted as a straight line equation with a slope of $(D_f - 2)$. Figure 16 (right) shows a double logarithmic plot of $\langle \Sigma_{gen} \rangle / \langle |\nabla \bar{c}| \rangle$ over the normalized filter size $\Delta/\delta_{th,st}$ for $\phi = 1.0$ and $t \times S_{L,st}/\delta_{th,st} = 1$. When the filter width is smaller than the stoichiometric flame thickness $\delta_{th,st}$, the variation of $\log(\langle \Sigma_{gen} \rangle / \langle |\nabla \bar{c}| \rangle)$ becomes increasingly nonlinear. For $\Delta \gg \delta_{th,st}$, the linear behavior expected from Eq. (17) becomes apparent and the fractal dimension

D_f can be calculated from the slope of a line fit. By repeating this procedure for successive timesteps and for all cases, the temporal evolution of D_f (Fig. 17) can be determined. Since the definition of D_f is mathematically related to the FSD or flame surface area A_f [Eq. (12a)], it is consistent that D_f evolves similarly to A_f as shown in Fig. 9. The upper half of Fig. 17 includes a comparison to the nonreactive case. For the lower half of Fig. 17, additional parameter variations at equivalence ratios between $\phi = 1.0$ and $\phi = 0.5$ have been performed, for which the parameters can be found in Table I. At the start of the simulation, the shock flattens the initially disturbed (Fig. 4) flame surface, reducing the fractal dimension to $D_f \approx 2$, or $\Xi \approx 1$. The fractal dimension then steeply increases to about 2.9 for $\phi = 1$ and 2.8 for $\phi = 0.5$. After the reshock, D_f increases further for $\phi = 0.5$ and reaches a maximum of ≈ 3 (≈ 2.9 for $\phi = 1.0$). The values obtained for D_f are limited to $D_f \leq 3$, since the highest theoretically obtainable value for the fractal dimension in three-dimensional space equals 3 [although higher values could be possible by interpreting Eq. (16) merely as a power-law model]. Especially in the middle sections of the simulation, values that reach that theoretical threshold should be interpreted with care, since they are subject to uncertainties due to sensitivities in the application of the post-processing methods (filtering methods, straight-line fit). The values for D_f reached toward the end are more conclusive as the values settle at about 2.4 ($\phi = 1$) and 2.7 ($\phi = 0.5$). The nonreactive case shows an interesting behavior, as in this case the fractal dimension initially evolves in a similar fashion as for $\phi = 1.0$ (the basis setup of the nonreactive case), but later settles at a similar value as the $\phi = 0.5$ case. This further highlights the strong influence of reactivity on the development of flame wrinkling.

The intersection of the straight-line fit with the line given by $\langle \Sigma_{gen} \rangle / \langle |\nabla \bar{c}| \rangle = 1$ in Fig. 16 yields the inner cutoff scale η_i . The development over time of the normalized inner cutoff scale $\eta_i/\delta_{th,st}$ is shown in Fig. 17, where the stoichiometric thermal flame thickness $\delta_{th,st}$ is used for normalization in both cases. The values of $\eta_i/\delta_{th,st}$ are only weakly dependent on the chosen equivalence ratio, since both cases show a similar temporal development for η_i . The values start at $\approx 0.75\delta_{th,st}$, then decrease to $\approx 0.5\delta_{th,st}$, before sharply increasing to a maximum of $1.5\delta_{th,st}$. Toward the end, the inner cutoff scale stabilizes at around $1\delta_{th,st} \pm 25\%$. The assumption of a (nearly) constant and

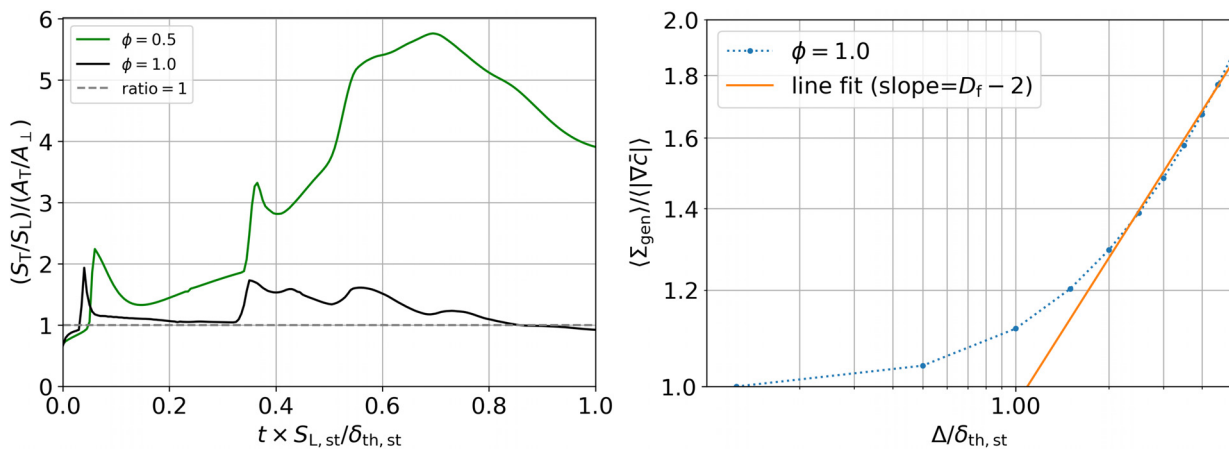


FIG. 16. Left: Deviation from the idealized Damköhler hypothesis for $\phi = 0.5$ and $\phi = 1.0$. Right: Double logarithmic plot of the volume-averaged wrinkling factor over the normalized filter size for $\phi = 1.0$ at $t \times S_{L,st}/\delta_{th,st} = 1$.

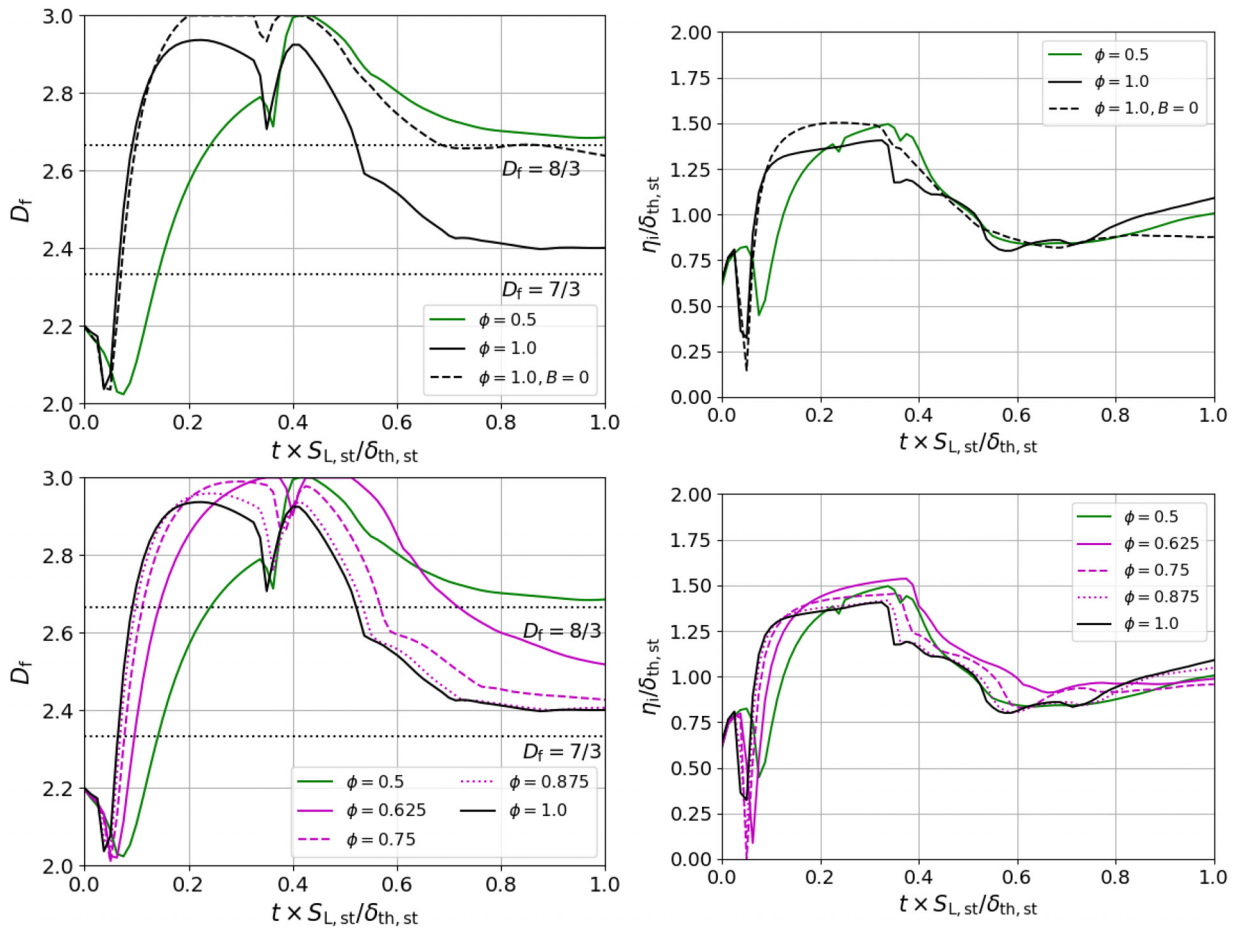


FIG. 17. Fractal dimension (left column) and inner cutoff scale (right column) for $\phi = 0.5$, $\phi = 1.0$ and nonreactive gas mixture (top) and a variation of equivalence ratios (bottom).

stoichiometry-independent η_i could be useful for simplified subgrid modeling approaches using Eq. (16), as only D_f has to be modeled or specified depending on the case. An additional parameter variation of the equivalence ratio is shown in the bottom half of Fig. 17. Since the corresponding equivalence ratios are distributed uniformly ($\Delta\phi = 0.125$), the nonlinear nature of transition between the lean and stoichiometric reference cases becomes apparent. The growth rate of D_f after the first shock interaction is dependent on the equivalence ratio and decreases with decreasing ϕ . This behavior is consistent with the development of the Mikaelian time scale³⁰ $t_m \sim \delta_{m,0}/\Delta v$, where $\delta_{m,0}$ is the initial mixing width and Δv is the velocity jump at the mixing interface caused by the shock. Decreasing ϕ causes $\delta_{m,0}$ to increase, since this value is heavily dependent on the initial flame thickness. For the first shock-flame interaction, Δv equals the postshock velocity, which decreases with decreasing ϕ , due to the dependence of the postshock velocity on the speed of sound $a_0 = \sqrt{\gamma R_s T_0}$, where R_s is mixture dependent. Both effects (increasing $\delta_{m,0}$; decreasing Δv) cause t_m to increase with decreasing ϕ , explaining the longer growth period of D_f after the first shock-flame interaction. For lower values of ϕ , there is less burnout of the emerging flame cusps;

therefore, higher values are reached for D_f . For $\phi = 0.5$ the reshock interaction takes place while D_f is still in its growth phase, causing a lower peak to be reached after the first shock-flame interaction. Toward the end of the simulation, the fractal dimension settles between values of $D_f = 7/3$ and $D_f = 8/3$, depending on the equivalence ratio. Here, a highly nonlinear dependency of D_f on ϕ becomes apparent. The parameter variation confirms the previous observation that the inner cutoff scale seems to be only weakly dependent on ϕ for the investigated cases.

The parametric analysis shown in Fig. 18 reaffirms the statements made in Secs. III and IV toward the importance of reactivity on the development of the RMI. While the previous variations A–C have no noticeable impact on D_f toward the end of the simulation, changing the laminar flame speed S_L (and therefore the reactivity) to the values for $\phi = 1.0$ leads to a sharp decline of D_f in case D.

The decrease in the equivalence ratio gives rise to reductions in S_L and increases in flame thickness, causing a shift from the strict flamelet regime toward a higher Karlovitz number regime. The end values reached for D_f (Figs. 17 and 18) increase from $\approx 7/3$ to $\approx 8/3$ when the equivalence ratio decreases. These values are consistent with

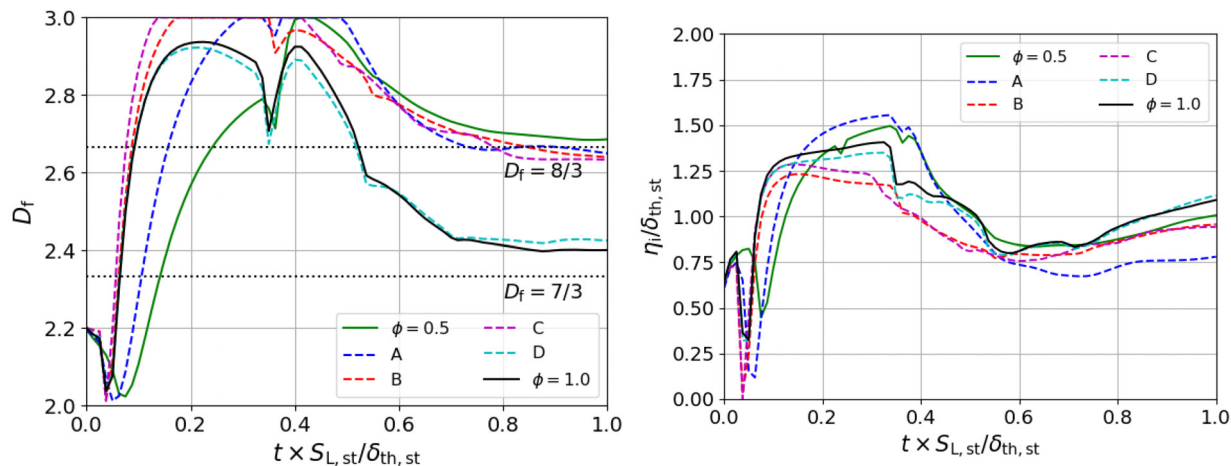


FIG. 18. Fractal dimension (left) and inner cutoff scale (right) for $\phi = 0.5$, $\phi = 1.0$ and cases A–D.

findings in the literature as in the flamelet regime Kerstein⁵⁹ suggests a fractal dimension of $7/3$, while the maximum D_f for a flame in the well-mixed regime,⁶⁰ as well as a passive scalar isosurface,⁶¹ has been found to be $8/3$.

V. SUMMARY AND CONCLUSION

In this study, the development of the RMI in lean ($\phi = 0.5$) and stoichiometric ($\phi = 1.0$) homogeneous H₂/air mixtures was investigated by performing compressible 3D simulations of shock-flame interactions with simple chemistry. As expected from theory, the interactions caused an increase in wrinkling and mixing as measured by the development of the flame surface area A_f and mixing width δ_m . The evolution of A_f after a shock interaction was divided into two separate phases. The first phase was characterized by an increase in A_f , caused by the build up of fresh gas cusps (first shock interaction) and the development of wrinkled structures (mainly after reshock). The second phase was heavily influenced by the reactivity and characterized by a decrease in A_f , due to transversal burnout of the fresh gas cusps and wrinkled structures. It was found that the equivalence ratio ϕ is an important factor in the development of the RMI, as it affects the reactivity, flame density gradient and speed of sound. The development of the mixing width δ_m was found to be influenced not only by the mixing (from wrinkling) of unburned and burned fluid but also by changes in the flame thickness itself. Similar to the behavior observed for A_f , the shock interactions initially caused an increase in δ_m , while the burnout reduced the mixing. At later times, it was found that increasing the equivalence ratio (up to stoichiometric conditions) can also increase δ_m , as large flame cusps propagate into the unburned gas mixture.

An investigation of the enstrophy transport terms was performed, where the baroclinic torque was identified as the most dominant contributor, accounting for up to 60% of the total integral enstrophy budget changes at moments of shock-flame interaction. For the investigated cases it was found that, following the shock interactions, the contributions of the vortex stretching, dissipation, and dilation can become quite significant, accounting for up to 80% of the

total integral enstrophy budget changes. This effect was found to be especially pronounced in the lean case, where vortex stretching alone accounted for up to 50% of the total integral enstrophy budget changes. The dissipation reduces the effect of the vortex stretching in the lean case and effectively cancels it out in the stoichiometric case. Finally, an investigation of the fractal behavior of the flame surface was conducted in the context of power-law based wrinkling factor modeling. Here, a highly nonlinear dependency of the fractal dimension D_f on ϕ was found, where decreasing ϕ causes an increase in D_f at late times. The inner cutoff scale however was found to be only weakly dependent on ϕ , reaching values close to the thermal flame thickness of the stoichiometric flame ($\pm 25\%$).

In the future, it will be worthwhile to extend this analysis toward fuel-rich mixtures, thus decreasing laminar burning velocity (compared to stoichiometric conditions), whereas other important influencing parameters like Lewis number and speed of sound increase further.

ACKNOWLEDGMENTS

The presented work is funded by the German Federal Ministry of Economic Affairs and Energy (BMWi) on the basis of a decision by the German Bundestag (Project No. 1501574) which is gratefully acknowledged. N.C. acknowledges financial and computational support from Engineering and Physical Sciences Research Council, UK (Grant No. EP/R029369/1).

DATA AVAILABILITY

The data that support the findings of this study are available from the corresponding author upon reasonable request.

REFERENCES

- R. D. Richtmyer, “Taylor instability in shock acceleration of compressible fluids,” *Commun. Pure Appl. Math.* **13**, 297–319 (1960).
- E. E. Meshkov, “Instability of the interface of two gases accelerated by a shock wave,” *Fluid Dyn.* **4**, 101–104 (1972).

- ³Lord Rayleigh, "Investigation of the character of the equilibrium of an incompressible heavy fluid of variable density," *Proc. London Math. Soc.* **s1-14**, 170–177 (1882).
- ⁴G. Taylor, "The instability of liquid surfaces when accelerated in a direction perpendicular to their planes. I," *Proc. R. Soc. London, Ser. A* **201**, 192–196 (1950).
- ⁵P. Ramaprabhu, V. Karkhanis, R. Banerjee, H. Varshochi, M. Khan, and A. G. Lawrie, "Evolution of the single-mode Rayleigh–Taylor instability under the influence of time-dependent accelerations," *Phys. Rev. E* **93**, 1–17 (2016).
- ⁶Y. Zhou, "Rayleigh–Taylor and Richtmyer–Meshkov instability induced flow, turbulence, and mixing. I," *Phys. Rep.* **720–722**, 1–136 (2017).
- ⁷Y. Zhou, "Rayleigh–Taylor and Richtmyer–Meshkov instability induced flow, turbulence, and mixing. II," *Phys. Rep.* **723–725**, 1–160 (2017).
- ⁸Y. Zhou, R. J. Williams, P. Ramaprabhu, M. Groom, B. Thornber, A. Hillier, W. Mostert, B. Rollin, S. Balachandar, P. D. Powell, A. Mahalov, and N. Attal, "Rayleigh–Taylor and Richtmyer–Meshkov instabilities: A journey through scales," *Physica D* (published online, 2021).
- ⁹J. Lindl, "Development of the indirect-drive approach to inertial confinement fusion and the target physics basis for ignition and gain," *Phys. Plasmas* **2**, 3933–4024 (1995).
- ¹⁰B. A. Remington, R. P. Drake, H. Takabe, and D. Arnett, "A review of astrophysics experiments on intense lasers," *Phys. Plasmas* **7**, 1641–1652 (2000).
- ¹¹A. M. Khokhlov, E. S. Oran, and G. O. Thomas, "Numerical simulation of deflagration-to-detonation transition: The role of shock–flame interactions in turbulent flames," *Combust. Flame* **117**, 323–339 (1999).
- ¹²G. Thomas, R. Bambrey, and C. Brown, "Experimental observations of flame acceleration and transition to detonation following shock–flame interaction," *Combust. Theory Modell.* **5**, 573–594 (2001).
- ¹³G. Ciccarelli, C. T. Johansen, and M. Parravani, "The role of shock–flame interactions on flame acceleration in an obstacle laden channel," *Combust. Flame* **157**, 2125–2136 (2010).
- ¹⁴V. N. Gamezo, T. Ogawa, and E. S. Oran, "Flame acceleration and DDT in channels with obstacles: Effect of obstacle spacing," *Combust. Flame* **155**, 302–315 (2008).
- ¹⁵S. B. Dorojevic, "Flame acceleration and explosion safety applications," *Proc. Combust. Inst.* **33**, 2161–2175 (2011).
- ¹⁶W. Breitung, C. Chan, S. Dorojevic, A. Eder, B. Gelfand, M. Heitsch, R. Klein, A. Mallikos, J. Shepherd, E. Studer, and P. Thibault, "Flame acceleration and deflagration-to-detonation transition in nuclear safety," Report No. NEA/CSNI/R(2000)7, 2000.
- ¹⁷G. Ciccarelli and S. Dorojevic, "Flame acceleration and transition to detonation in ducts," *Prog. Energy Combust. Sci.* **34**, 499–550 (2008).
- ¹⁸J. Hasslberger, "Numerical simulation of deflagration-to-detonation transition on industry scale," Ph.D. thesis (Technical University Munich, 2017).
- ¹⁹J. Yanez, M. Kuznetsov, and A. Souto-Iglesias, "An analysis of the hydrogen explosion in the Fukushima-Daiichi accident," *Int. J. Hydrogen Energy* **40**, 8261–8280 (2015).
- ²⁰K. W. Jenkins and R. S. Cant, "Direct numerical simulation of turbulent flame kernels," in *Recent Advances in DNS and LES*, edited by D. Knight and L. Sakell (Springer Netherlands, Dordrecht, 1999), pp. 191–202.
- ²¹R. C. Rogers and W. Chinitz, "Using a global hydrogen-air combustion model in turbulent reacting flow calculations," *AIAA J.* **21**, 586–592 (1983).
- ²²T. Lu and C. K. Law, "Toward accommodating realistic fuel chemistry in large-scale computations," *Prog. Energy Combust. Sci.* **35**, 192–215 (2009).
- ²³C. Dopazo and E. E. O'Brien, "Functional formulation of nonisothermal turbulent reactive flows," *Phys. Fluids* **17**, 1968 (1974).
- ²⁴S. Bane, J. Ziegler, and J. Shepherd, "Development of one-step chemistry models for flame and ignition simulation," GALCIT Report GALCITFM: 2010.002, 2010, p. 53.
- ²⁵A. A. Wray, "Minimal storage time advancement schemes for spectral methods," NASA Ames Research Center, California, Report No. MS 202, 1990.
- ²⁶G.-S. Jiang and C.-W. Shu, "Efficient implementation of weighted ENO schemes," *J. Comput. Phys.* **126**, 202–228 (1996).
- ²⁷C.-W. Shu, "Essentially non-oscillatory and weighted essentially non-oscillatory schemes for hyperbolic conservation laws," in *Advanced Numerical Approximation of Nonlinear Hyperbolic Equations* (Springer, 1998), pp. 325–432.
- ²⁸T. Poinsot and D. Veynante, *Theoretical and Numerical Combustion* (Edwards, London, 2005).
- ²⁹V. K. Tritschler, S. Hickel, X. Y. Hu, and N. A. Adams, "On the Kolmogorov inertial subrange developing from Richtmyer–Meshkov instability," *Phys. Fluids* **25**, 071701 (2013).
- ³⁰K. O. Mikaelian, "Extended model for Richtmyer–Meshkov mix," *Phys. D* **240**, 935–942 (2011).
- ³¹J. D. Anderson, *Fundamentals of Aerodynamics*, McGraw-Hill Series in Aeronautical and Aerospace Engineering (McGraw Hill Education, 2017).
- ³²G. Dimonte and M. Schneider, "Density ratio dependence of Rayleigh–Taylor mixing for sustained and impulsive acceleration histories," *Phys. Fluids* **12**, 304–321 (2000).
- ³³M. M. Mansoor, S. M. Dalton, A. A. Martinez, T. Desjardins, J. J. Charonko, and K. P. Prestridge, "The effect of initial conditions on mixing transition of the Richtmyer–Meshkov instability," *J. Fluid Mech.* **904**, A3 (2020).
- ³⁴B. Thornber, J. Griffond, O. Poujade, N. Attal, H. Varshochi, P. Bigdelou, P. Ramaprabhu, B. Olson, J. Greenough, Y. Zhou, O. Schilling, K. A. Garside, R. J. R. Williams, C. A. Batha, P. A. Kuchugov, M. E. Ladonkina, V. F. Tishkin, N. V. Zmitrenko, V. B. Rozanov, and D. L. Youngs, "Late-time growth rate, mixing, and anisotropy in the multimode narrowband Richtmyer–Meshkov instability: The θ -group collaboration," *Phys. Fluids* **29**, 105107 (2017).
- ³⁵D. G. Goodwin, R. L. Speth, H. K. Moffat, and B. W. Weber, <https://www.cantera.org> for Cantera: An object-oriented software toolkit for chemical kinetics, thermodynamics, and transport processes, version 2.4.0, 2018.
- ³⁶J. K. Bechtold and M. Matalon, "The dependence of the Markstein length on stoichiometry," *Combust. Flame* **127**, 1906–1913 (2001).
- ³⁷E. E. O'Brien, "Turbulent mixing of two rapidly reacting chemical species," *Phys. Fluids* **14**, 1326 (1971).
- ³⁸M. Klein, A. Herbert, H. Kosaka, B. Böhm, A. Dreizler, N. Chakraborty, V. Papapostolou, H. G. Im, and J. Hasslberger, "Evaluation of flame area based on detailed chemistry DNS of premixed turbulent hydrogen-air flames in different regimes of combustion," *Flow, Turbul. Combust.* **104**, 403–419 (2020).
- ³⁹V. K. Tritschler, B. J. Olson, S. K. Lele, S. Hickel, X. Y. Hu, and N. A. Adams, "On the Richtmyer–Meshkov instability evolving from a deterministic multi-mode planar interface," *J. Fluid Mech.* **755**, 429–462 (2014).
- ⁴⁰M. Boger, D. Veynante, H. Bougahem, and A. Trouv , "Direct numerical simulation analysis of flame surface density concept for large eddy simulation of turbulent premixed combustion," *Symp. (Int.) Combust.* **27**, 917–925 (1998).
- ⁴¹D. Sharp, "An overview of Rayleigh–Taylor instability," *Phys. D* **12**, 3–18 (1984).
- ⁴²A. N. Lipatnikov, J. Chomiak, V. A. Sabelnikov, S. Nishiki, and T. Hasegawa, "Unburned mixture fingers in premixed turbulent flames," *Proc. Combust. Inst.* **35**, 1401–1408 (2015).
- ⁴³A. Y. Poludnenko, "Pulsating instability and self-acceleration of fast turbulent flames," *Phys. Fluids* **27**, 014106 (2015).
- ⁴⁴N. Attal and P. Ramaprabhu, "Numerical investigation of a single-mode chemically reacting Richtmyer–Meshkov instability," *Shock Waves* **25**, 307–328 (2015).
- ⁴⁵R. Yu and A. N. Lipatnikov, "Direct numerical simulation study of statistically stationary propagation of a reaction wave in homogeneous turbulence," *Phys. Rev. E* **95**, 063101 (2017).
- ⁴⁶M. Bambauer, J. Hasslberger, and M. Klein, "Direct numerical simulation of the Richtmyer–Meshkov instability in reactive and nonreactive flows," *Combust. Sci. Technol.* **192**, 2010–2018 (2020).
- ⁴⁷A. N. Lipatnikov, S. Nishiki, and T. Hasegawa, "A direct numerical simulation study of vorticity transformation in weakly turbulent premixed flames," *Phys. Fluids* **26**, 105104 (2014).
- ⁴⁸N. Chakraborty, I. Konstantinou, and A. Lipatnikov, "Effects of Lewis number on vorticity and enstrophy transport in turbulent premixed flames," *Phys. Fluids* **28**, 015109 (2016).
- ⁴⁹W. Cabot, "Comparison of two- and three-dimensional simulations of miscible Rayleigh–Taylor instability," *Phys. Fluids* **18**, 045101 (2006).
- ⁵⁰H. C. Liu, B. Yu, H. Chen, B. Zhang, H. Xu, and H. Liu, "Contribution of viscosity to the circulation deposition in the Richtmyer–Meshkov instability," *J. Fluid Mech.* **895**, A10 (2020).
- ⁵¹C. Fureby, "A fractal flame-wrinkling large eddy simulation model for premixed turbulent combustion," *Proc. Combust. Inst.* **30**, 593–601 (2005).

- ⁵²R. Knikker, D. Veynante, and C. Meneveau, “A dynamic flame surface density model for large eddy simulation of turbulent premixed combustion,” *Phys. Fluids* **16**, L91–L94 (2004).
- ⁵³O. Gülder, “Inner cutoff scale of flame surface wrinkling in turbulent premixed flames,” *Combust. Flame* **103**, 107–114 (1995).
- ⁵⁴G. Damköhler, “Der einfluss der turbulenz auf die flammengeschwindigkeit in gasgemischen,” *Z. Elektrochem. Angew. Phys. Chem.* **46**, 601–626 (1940).
- ⁵⁵N. Chakraborty and M. Klein, “*A priori* direct numerical simulation assessment of algebraic flame surface density models for turbulent premixed flames in the context of large eddy simulation,” *Phys. Fluids* **20**, 085108 (2008).
- ⁵⁶N. Chakraborty, D. Alwazzan, M. Klein, and R. S. Cant, “On the validity of Damköhler’s first hypothesis in turbulent Bunsen burner flames: A computational analysis,” *Proc. Combust. Inst.* **37**, 2231–2239 (2019).
- ⁵⁷N. Chakraborty, L. Wang, and M. Klein, “Streamline segment statistics of premixed flames with nonunity Lewis numbers,” *Phys. Rev. E: Stat., Nonlinear, Soft Matter Phys.* **89**, 033015 (2014).
- ⁵⁸F. Gouldin, K. Bray, and J.-Y. Chen, “Chemical closure model for fractal flamelets,” *Combust. Flame* **77**, 241–259 (1989).
- ⁵⁹A. R. Kerstein, “Fractal dimension of turbulent premixed flames,” *Combust. Sci. Technol.* **60**, 441–445 (1988).
- ⁶⁰E. R. Hawkes, O. Chatakonda, H. Kolla, A. R. Kerstein, and J. H. Chen, “A petascale direct numerical simulation study of the modelling of flame wrinkling for large-eddy simulations in intense turbulence,” *Combust. Flame* **159**, 2690–2703 (2012).
- ⁶¹B. B. Mandelbrot, “On the geometry of homogeneous turbulence, with stress on the fractal dimension of the iso-surfaces of scalars,” *J. Fluid Mech.* **72**, 401 (1975).